

Supernova Rates and Luminosity Functions from ASAS-SN III: Over a Decade of Type Ia SNe and Their Subtypes

D. D. DESAI¹, B. J. SHAPPEE¹, C. S. KOCHANEK^{2,3}, K. Z. STANEK^{2,3}, C. ASHALL¹, J. F. BEACOM^{1,4,2,3},
C. R. BURNS⁵, A. DO⁶, SUBO DONG^{7,8,9}, W. B. HOOGENDAM¹, J. LU¹⁰, T. PESSI¹¹, J. L. PRIETO^{12,13},
AND T. A. THOMPSON^{12,4,3}

¹ Institute for Astronomy, University of Hawai‘i, 2680 Woodlawn Drive, Honolulu, HI 96822, USA

² Department of Astronomy, The Ohio State University, 140 West 18th Avenue, Columbus, OH 43210, USA

³ Center for Cosmology and AstroParticle Physics, The Ohio State University, 191 West Woodruff Avenue, Columbus, OH 43210, USA

⁴ Department of Physics, The Ohio State University, 191 West Woodruff Avenue, Columbus, OH 43210, USA

⁵ Observatories of the Carnegie Institution for Science, 813 Santa Barbara Street, Pasadena, CA 91101, USA

⁶ Institute of Astronomy and Kavli Institute for Cosmology, Madingley Road, Cambridge, CB3 0HA, UK

⁷ Department of Astronomy, School of Physics, Peking University, 5 Yiheyuan Road, Haidian District, Beijing 100871, People’s Republic of China

⁸ Kavli Institute of Astronomy and Astrophysics, Peking University, 5 Yiheyuan Road, Haidian District, Beijing 100871, People’s Republic of China

⁹ National Astronomical Observatories, Chinese Academy of Science, 20A Datun Road, Chaoyang District, Beijing 100101, China

¹⁰ Department of Physics & Astronomy, Michigan State University, East Lansing, MI 48824, USA

¹¹ European Southern Observatory, Alonso de Córdoba 3107, Vitacura, Casilla 19001, Santiago, Chile

¹² Instituto de Estudios Astrofísicos, Facultad de Ingeniería y Ciencias, Universidad Diego Portales, Av. Ejército Libertador 441, Santiago, Chile and

¹³ Millennium Institute of Astrophysics MAS, Nuncio Monsenor Sotero Sanz 100, Off. 104, Providencia, Santiago, Chile

Version February 3, 2026

ABSTRACT

We present volumetric rates and luminosity functions (LFs) of Type Ia supernovae (SNe Ia) from the All-Sky Automated Survey for Supernovae (ASAS-SN), covering the 11-year period from 2014 to 2024. By combining the 2014–2017 *V*-band sample with the 2018–2024 *g*-band sample, we construct a large statistical dataset of 1776 SNe Ia. We compute completeness corrections based on injection-recovery simulations of the ASAS-SN light curves, taking into account the variations in light curve shapes. For our standard sample ($M_{g,\text{peak}} < -16.0$ mag), we extract a total volumetric SN Ia rate of $R_{\text{tot}} = (2.55 \pm 0.12) \times 10^4 \text{ yr}^{-1} \text{ Gpc}^{-3} h_{70}^3$ at a median redshift of $z = 0.029$. With a statistical uncertainty of 4.7%, this is the most precise local measurement to date. While the “normal” SNe Ia account for $(92.7 \pm 1.9)\%$ of this rate, the total LF reveals immense diversity, with $M_{g,\text{peak}}$ spanning over five magnitudes. The LF of SNe Iax is also broad and rises toward lower luminosities, resulting in a likely lower limit of $(4.3 \pm 1.8)\%$ of the total rate. We place strong constraints on the rate of SNe Ia-CSM, finding they account for only $(0.036 \pm 0.017)\%$ of the total local rate. Finally, we find that the low-luminosity 02es-like SNe are 7 ± 5 times more common than the luminous 03fg-like SNe. This places demographic constraints on models proposing a physical continuum for these two subtypes, implying that any common channel for the two classes must strongly favor lower-luminosity explosions.

Subject headings: supernovae: general – methods: data analysis – surveys

1. INTRODUCTION

The rates of Type Ia supernovae (SNe Ia) and their subtypes are fundamental observables that link stellar evolution to galactic chemical enrichment and cosmology. Precise measurement of these rates constrains progenitor population models, traces the cosmic history of star formation, and quantifies the production of iron-peak elements and Galactic positrons (e.g., Raiteri et al. 1996; Matteucci & Recchi 2001; Horiuchi & Beacom 2010; Maoz & Mannucci 2012; Desai et al. 2025). Historically, rate measurements relied on galaxy-targeted searches or heterogeneous compilations, which suffer from small sample sizes and complex selection biases (e.g., Cappellaro et al. 1999; Li et al. 2011b). Modern, wide-field, untargeted surveys have transformed this landscape and constructed statistical samples, providing more robust

measurements of the local SN Ia rate (e.g., Frohmaier et al. 2019; Perley et al. 2020; Srivastav et al. 2022; Sharon & Kushnir 2022; Desai et al. 2024).

The All-Sky Automated Survey for Supernovae (ASAS-SN; Shappee et al. 2014; Kochanek et al. 2017; Hart et al. 2023) provides a uniquely powerful data set. Since 2014, ASAS-SN has observed the entire visible sky with a daily-to-few-day cadence. It remained the only survey with this capability until 2022, when ATLAS expanded its coverage to the Southern hemisphere. ASAS-SN’s untargeted strategy and shallow depth ($g \lesssim 18.5$ mag) naturally produces a sample of bright, nearby transients with high spectroscopic completeness, as nearly every discovered object is bright enough for classification with modest telescope resources (Chen et al. 2022; Tucker et al. 2022). During the 2014–2017 *V*-band phase, ASAS-SN was nearly spectroscopically complete (Holoién et al. 2017a,b,c, 2019). While the subsequent *g*-band survey (2018–2024) has a slightly

lower average spectroscopic completeness ($\sim 81\%$, in part due to issues related to the COVID-19 pandemic), the deeper limiting magnitude and longer time baseline increase the sample by a factor of 3.4 over the V -band sample (e.g., Neumann et al. 2023).

This paper is the third in a series from the ASAS-SN team establishing benchmark local transient rates. In Paper I (Desai et al. 2024, hereafter D24), we established our methodology using the 2014–2017 V -band SN Ia sample and found a total volumetric rate of $R_{\text{tot},V} = (2.28 \pm 0.20) \times 10^4 \text{ yr}^{-1} \text{ Gpc}^{-3} h_{70}^3$, a measurement that is statistically precise and systematically robust due to the high completeness of the V -band sample. Paper II applied this framework to the core-collapse SNe from the same era (Pessi et al. 2025).

Here, we analyze the larger and deeper SN Ia sample from the ASAS-SN g -band survey, covering the years 2018 through 2024. By combining this new sample with the V -band sample, we more than quadruple the total sample size. This extended dataset provides the statistical power necessary to dissect the diversity of the SN Ia population. We provide robust volumetric rates and luminosity functions (LFs) for the major SN Ia subtypes, including the 91T-like (e.g., Filippenko et al. 1992; Phillips et al. 1992, 2024), 02es-like (e.g., Ganeshalingam et al. 2012), 03fg-like (e.g., Howell et al. 2006; Ashall et al. 2021), Iax (e.g., Foley et al. 2013; Jha 2017), and Ia-CSM events (e.g., Silverman et al. 2013; Sharma et al. 2023). Quantifying the relative rates of these subtypes is essential for understanding the overall SN Ia delay-time distribution and distinguishing between progenitor channels (e.g., Maoz et al. 2010, 2014; White et al. 2015; Hoogendam et al. 2024; Ruiter & Seitenzahl 2025).

In Section 2, we describe the g -band SN Ia sample and our light-curve fitting procedure. In Section 3, we detail the methodology for our rate calculations and combining the V - and g -band samples. We present our results on the volumetric rates in Section 4 and the luminosity functions in Section 5. Finally, in Section 6, we summarize our conclusions and their implications. Throughout this analysis, we adopt a flat Λ CDM cosmology with $H_0 = 70 \text{ km s}^{-1} \text{ Mpc}^{-1}$ and $\Omega_{m,0} = 0.3$.

2. THE SUPERNOVA SAMPLE

The SN sample in this paper builds upon the ASAS-SN catalogues presented in Holoiu et al. (2017a,b,c, 2019) and Neumann et al. (2023). Our added sample covers SNe discovered or recovered by ASAS-SN in the g -band between UTC 2021-01-01 and UTC 2024-12-31. To ensure uniformity, the 2018–2020 sample from Neumann et al. (2023) is reanalyzed here to provide updated light-curve fits and peak magnitudes consistent with the methods used in D24 and Pessi et al. (2025).

Since our time period extends beyond that of Neumann et al. (2023), we compiled a list of SNe discovered by ASAS-SN from the Transient Name Server¹ (TNS) and the archival ASAS-SN supernova page². To identify SNe discovered by other surveys but independently recovered in ASAS-SN data, we cross-matched all transients re-

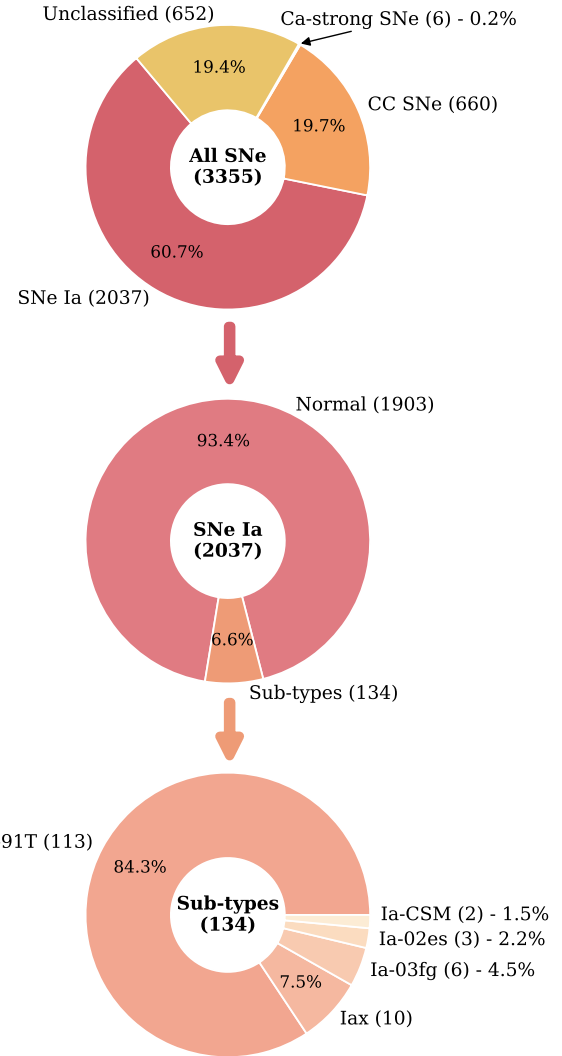


FIG. 1.— Fractions and numbers of all SNe discovered or recovered by ASAS-SN in g -band from UTC 2018-01-01 to UTC 2024-12-31.

ported to TNS with the ASAS-SN transient archive³. This combined sample of discoveries and recoveries was then filtered to remove non-supernova transients, such as cataclysmic variables, novae, active galactic nuclei, and tidal disruption events. This process resulted in a list of 2703 spectroscopically classified SNe and 1685 unclassified transients. For the unclassified transients, we retained candidates that had a potential host galaxy within a $1'$ radius and a light curve morphologically consistent with our supernova templates. We further vetted these candidates by cross-matching their positions with stellar catalogues from Gaia, Pan-STARRS, TESS, and GALEX, removing any that had a Galactic stellar counterpart within a $5''$ radius, thus leaving 652 unclassified potential SNe in our sample.

We update the classifications for several objects in our sample. ASASSN-18ro (SN 2018evt), originally classified as SN Ia, is updated to SN Ia-CSM (Dong et al. 2018;

¹ <https://www.wis-tns.org/>

² https://www.astronomy.ohio-state.edu/asassn/sn_list.html

³ <https://www.astronomy.ohio-state.edu/asassn/transients.html>

Yang et al. 2023), and SN 2022esa, originally classified as SN Ia-CSM, is updated to SN Ic-CSM (Griffith et al. 2025; Maeda et al. 2025). For 11 SNe in our sample classified as SN Ia-pec on TNS, we examine the spectra to determine more appropriate subtypes: SNe 2019ein, 2020dju, 2021ebb, 2022bbt, and 2022aana are normal SNe Ia; SNe 2014dt, 2019omz, and 2020rea are SNe Iax; SNe 2018las, 2021qce, and 2022obk are SNe Ia-91T-like. We remove AT 2020adgm (ASASSN-20qc) from the sample for being an ambiguous nuclear transient (Pasham et al. 2024). Our g -band sample comprises 3355 supernovae discovered or recovered by ASAS-SN in the years 2018 to 2024, of which 80.6% are spectroscopically classified. Figure 1 shows the division of these 3355 SNe into SN types, with 2037 spectroscopically classified SNe Ia.

We note that distinguishing 91T-like events from the closely related 1999aa-like events and other Branch shallow-silicon supernovae is difficult without a spectral time series (Phillips et al. 2022). Consequently, our 91T-like sample likely includes a fraction of these related subtypes. Furthermore, we define the “normal” SN Ia population to encompass both the Core Normal (CN) and Broad Line (BL) Branch subtypes. We also categorize the subluminous 91bg-like subclass and transitional events from TNS as normal SNe Ia, as recent analyses of these events and the use of the color-stretch parameter s_{BV} demonstrate that they transition smoothly from the luminous population rather than forming a distinct, peculiar class (Ashall et al. 2018; Burns et al. 2018; Gall et al. 2018; Phillips et al. 2025).

To control systematic uncertainties in the peak magnitudes, we uniformly refit the ASAS-SN g -band light curves for all SNe using a suite of subtype-specific templates. The fits are performed in flux space using a χ^2 minimization routine. For normal SNe Ia, we use the g -band flux templates from the Carnegie Supernova Project (CSP; Burns et al. 2018), which are extracted using SNoPy (Burns et al. 2011), and incorporate the dependence of absolute magnitude on s_{BV} . The single-band nature of the ASAS-SN light curves precludes color information, leaving the fitted s_{BV} values poorly constrained.

For the peculiar subtypes (91T-like, Iax, 03fg-like, 02es-like, and Ia-CSM), we employ custom templates derived from Gaussian Process fits to the light curves of representative, well-observed events from the literature (e.g., Krisciunas et al. 2017; Parrent et al. 2016; Dimitriadis et al. 2023; Xi et al. 2024; Yang et al. 2023). Detailed descriptions of these templates and the specific SNe used to construct them are provided in Appendix A. For unclassified SNe, we fit all available templates and select the one that provides the best fit to the peak and the light-curve morphology. To reject outlier data points, we employ a two-pass sigma-clipping procedure: an initial 15σ clip followed by a final 5σ clip on the residuals of the best-fit model. We determine uncertainties on the best-fit parameters using Monte Carlo methods.

We compute absolute magnitudes for all SNe using

$$M_g = m_g - \mu - A_{g,\text{MW}} - K_g(z), \quad (1)$$

where m_g is the apparent g -band peak magnitude from our light-curve fits, μ is the distance modulus for the supernova redshift obtained using the `astropy.cosmology` package (Astropy Collaboration et al. 2013, 2018), and

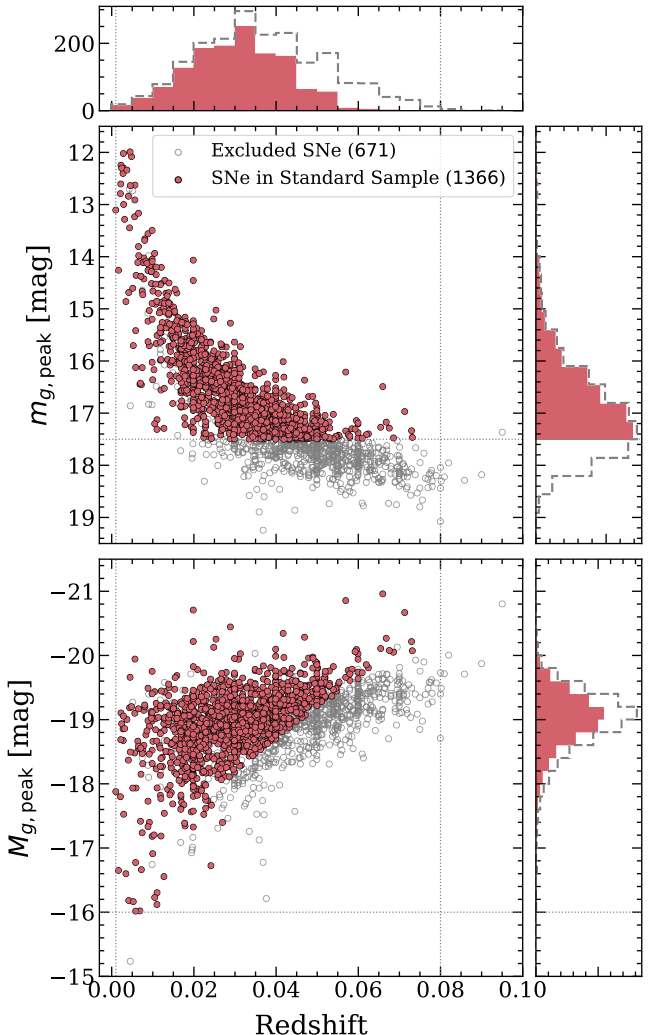


FIG. 2.— Peak apparent (top) and absolute (bottom) magnitude versus redshift distributions of the 2037 SNe Ia discovered or recovered by ASAS-SN (gray). The filled circles and filled histograms show our g -band standard sample of 1366 SNe Ia. Open gray points are the SNe excluded by our standard cuts on peak absolute magnitude $M_{g,\text{peak}}$, Galactic latitude b , peak apparent magnitude $m_{g,\text{peak}}$, and redshift z , as marked by the gray dotted lines.

$A_{g,\text{MW}}$ is the Milky Way extinction from Schlafly & Finkbeiner (2011). When available, we use redshift-independent distance moduli for $\mu < 32$ mag ($z < 0.006$) due to the significance of peculiar velocities at these low redshifts (for more details, see Appendix B). The K-correction, $K_g(z)$, is computed using SNoPy (Burns et al. 2011) with the spectral templates from Hsiao et al. (2007). We do not apply a correction for host-galaxy extinction because the single-band ASAS-SN photometry does not provide the color information required to do so robustly. While the light curve fits yield peak apparent magnitudes with statistical uncertainties of ~ 0.05 mag, the systematic uncertainty in the absolute peak magnitudes is dominated by errors in the distance estimates and host-galaxy extinction.

For our standard analysis, we apply several cuts to the full sample of 2037 SNe Ia to create a statistically robust subset. We use a limiting Galactic lati-

TABLE 1

The g -band sample of Type Ia SNe discovered or recovered by ASAS-SN from UTC 2018-01-01 to UTC 2024-12-31.

IAU Name	ASASS-SN Name	RA [deg]	Dec [deg]	Type	z	$t_{g,\text{peak}}^a$ [JD]	$m_{g,\text{peak}}^a$ [mag]	$M_{g,\text{peak}}^b$ [mag]	Disc./Rec. ^c
2018eml	—	236.5296	29.7335	Ia	0.0316	2458343.06	16.67	-19.08	R
2018hme	ASASSN-18yf	143.9137	-17.3864	Ia	0.0141	2458412.98	15.72	-18.50	D
2019aos	ASASSN-19co	198.1609	-30.0234	Ia-91T-like	0.0300	2458529.85	16.74	-19.01	D
2019hma	—	157.2444	8.4795	Ia	0.0470	2458652.47	17.55	-19.06	R
2020eee	—	180.0149	10.3723	Ia	0.0710	2458927.11	18.13	-19.39	R
2020hvf	—	170.3602	3.0147	Ia-03fg-like	0.0058	2458979.08	12.63	-19.94	R
2021vpv	—	335.5216	19.8767	Ia-91T-like	0.0400	2459446.02	16.90	-19.43	R
2021wjb	ASASSN-21qf	300.2080	-38.5772	Ia	0.0200	2459452.06	15.79	-19.09	D
2022eyw	—	190.9999	62.3301	Iax	0.0090	2459673.76	15.63	-17.34	R
2022yz	—	35.3532	30.1326	Ia	0.0400	2459608.76	16.84	-19.59	R
2023vha	—	11.3832	31.0076	Ia	0.0820	2460246.74	17.95	-20.00	R
2023yma	—	13.0572	44.3324	Ia	0.0178	2460286.95	15.71	-19.06	R
2024jeg	—	198.4803	21.5768	Ia	0.0459	2460462.23	17.42	-19.10	R
2024nnu	ASASSN-24ei	23.7599	41.2482	Ia	0.0170	2460493.42	15.67	-18.83	D

NOTE. — This table of 2037 SNe Ia is available in its entirety in a machine-readable form in the online journal. A portion is shown here for guidance regarding its form and content.

^a Peak apparent magnitude and time of peak are derived from refitting ASAS-SN light curves with subtype-specific templates.

^b Peak absolute magnitudes are computed using $m_{g,\text{peak}}$ and Equation 1.

^c Indicates whether the SN was discovered by ASAS-SN (D) or independently recovered in ASAS-SN data (R).

tude of $|b| > 15^\circ$, a limiting peak absolute magnitude of $M_{g,\text{peak}} < -16.0$ mag, and a limiting peak apparent magnitude of $m_{g,\text{peak}} < 17.5$ mag, where our survey completeness is well-characterized. These cuts are justified in Section 4.1. We restrict the redshift range to $0.001 < z < 0.08$. After applying these cuts, our final g -band sample for rate calculations consists of 1366 supernovae. Their distribution in $m_{g,\text{peak}}$, $M_{g,\text{peak}}$, and redshift is shown in Figure 2. The properties of the full g -band sample of 2037 SNe Ia are listed in Table 1.

To leverage the full 11-year baseline of ASAS-SN, we combine this g -band sample with the V -band sample from Paper I (D24). We apply the same selection criteria to the 2014–2017 data for Galactic latitude, absolute magnitude, and redshift, with the only difference being the apparent magnitude limit ($m_{V,\text{peak}} < 17.0$ mag versus $m_{g,\text{peak}} < 17.5$ mag). These cuts contribute an additional 410 SNe Ia from the V -band era. The final combined dataset used for our standard rate analysis therefore consists of 1776 SNe Ia.

3. RATE COMPUTATIONS

We follow the approach of Papers I (D24) and II (Pessi et al. 2025) to compute the volumetric rates, using injection-recovery simulations to estimate the survey completeness as a function of magnitude.

Papers I and II used a simple piecewise function for the probability of detection (p) in any given epoch as a function of signal-to-noise ratio (SNR). While this was sufficient for the V -band data through 2017, the detection efficiency in later years (g -band) varied due to operational changes and resource constraints related to the COVID-19 pandemic and other factors. To account for this, we adopt a more sophisticated parameterization for the detection efficiency from 2018 to 2024. In general, the detection probability is low for low SNR, rises, and then saturates at high SNR. We model this behavior using a cumulative skew-normal distribution with height

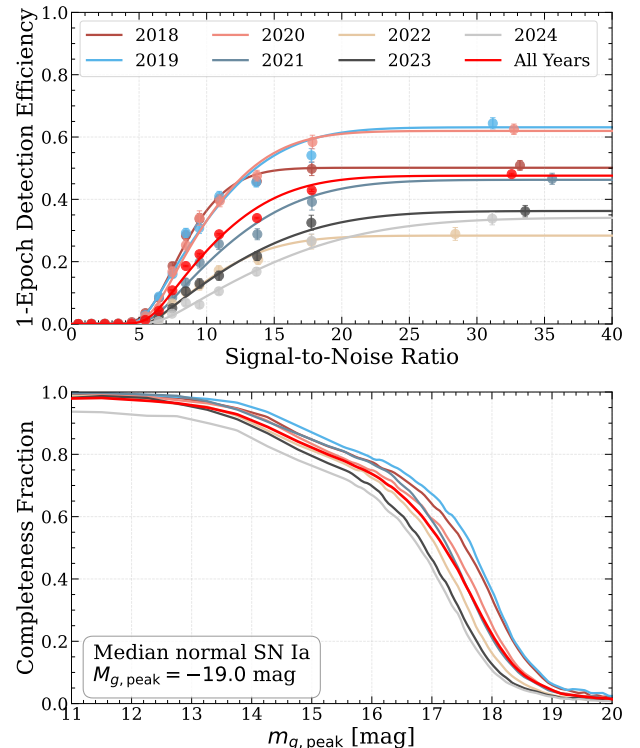


FIG. 3.— The ASAS-SN g -band detection performance. *Top*: The probability of flagging a source as a detection in a *single* epoch as a function of SNR for each year. The colored points show binned efficiency estimates from the data, and the solid lines are the best fits from Equation 2. *Bottom*: The completeness fraction as a function of peak apparent magnitude per year for a typical normal SN Ia ($M_{g,\text{peak}} = -19.0$ mag). While the single-epoch efficiency (top) saturates much below unity, the high cadence of ASAS-SN ensures a higher total detection probability for brighter transients (bottom).

TABLE 2
Yearly and aggregate best-fit parameters for the detection probability defined in Equation 2.

Year	H	μ	σ	α
2018	0.50	5.68	3.95	3.60
2019	0.63	5.23	6.68	10.13
2020	0.62	5.71	5.87	6.76
2021	0.46	5.85	7.58	8.82
2022	0.28	6.06	5.98	7.37
2023	0.36	5.82	8.61	18.41
2024	0.34	6.49	10.53	9.72
2018 – 2024	0.48	5.69	6.50	7.71

H , center μ , width σ , and skewness α , given by

$$p = \frac{H}{\sigma} \int_{-\infty}^{\text{SNR}} \phi\left(\frac{x-\mu}{\sigma}\right) \left[1 + \text{erf}\left(\frac{\alpha(x-\mu)}{\sigma\sqrt{2}}\right)\right] dx \quad (2)$$

where ϕ is the probability density function of the standard normal distribution.

Based on all g -band observations of supernovae (discovered, recovered, and missed), we fit Equation 2 to the detection efficiency as a function of SNR for each year separately. Figure 3 (top) shows these fits, and Table 2 presents the best-fit parameters for each year. Although this represents the probability of detection per observation, the high cadence of ASAS-SN (1 – 2 days in the g -band) renders the probability of missing a bright SN negligible. Even if Equation 2 underestimates p for bright SNe, these objects have many detection trials (n), and the overall detection probability, $1 - (1 - p)^n$, rapidly converges to unity. For example, with $n = 5$ trials, the probability of detection for a bright SN is 96.2% for an average $p = 0.48$, compared to nearly 100.0% for an idealized $p = 0.95$. This total completeness fraction per year is demonstrated for a typical SN Ia in the bottom panel of Figure 3. This completeness includes both weather and seasonal losses.

We performed injection-recovery simulations by drawing $N_{\text{LC}} = 100,000$ random ASAS-SN g -band light curves. For each trial, we injected a synthetic SN light curve based on the templates for each subtype and peak absolute magnitude. For normal SNe Ia, we used the CSP-II templates (Burns et al. 2018), which relate the peak absolute magnitude to the color-stretch parameter s_{BV} . Each synthetic observation was then flagged as a “detection” or “non-detection” based on the probability from Equation 2. A trial SN was considered detected if at least one epoch was flagged as a detection. We conducted a total of $M = 100 N_{\text{LC}}$ trials, resulting in a detection fraction of $F_1 = N/M$ divided by year, where N is the number of detected trials. The resulting completeness fractions for all years combined are shown for each of our SN Ia templates in Figure 4.

As in Papers I and II, we introduce a second correction factor, $F_2(M_{g,\text{peak}}) = V(z_{\text{lim}}(M_{g,\text{peak}}))/V(z_{\text{max}})$, to account for the varying maximum redshift, z_{lim} , used for different absolute magnitudes in the simulations. This factor normalizes the detection volume to that of our maximum redshift z_{max} .

Finally, since the spectroscopic completeness varies by up to $\sim 20\%$ with year and apparent magnitude, we

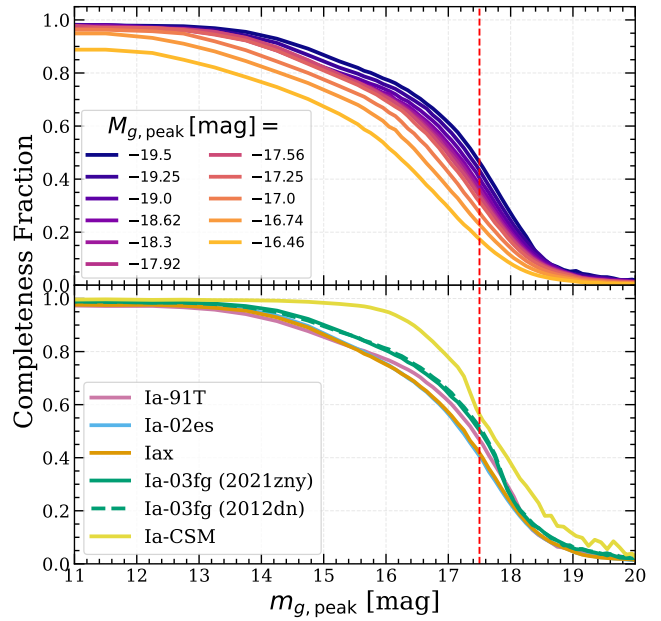


FIG. 4.— *Top*: Completeness fraction (F_1) for all years combined for normal SNe Ia. *Bottom*: Completeness fraction (F_1) for all years combined for other subtypes of SNe Ia. The dashed red line marks the standard limiting magnitude of $g = 17.5$ mag.

adopt a third correction factor, F_3 . This factor is the fraction of SNe with spectroscopic classifications in a given year and apparent magnitude bin. It assumes that the intrinsic distribution of unclassified SNe is the same as that of classified SNe within a given magnitude bin, which is a reasonable approximation for this work. We discuss spectroscopic completeness further in Appendix C. The final statistical weight for the i^{th} observed SN is $w_{i,g} = (F_{1,i} F_{2,i} F_{3,i})^{-1}$. The volumetric SN rate is then

$$R_g = \frac{\sum_{i=1}^N w_{i,g}}{V \Delta t_g (1 - \sin b_{\text{lim}})}, \quad (3)$$

where $\Delta t_g = 7.0$ yr is the time span from UTC 2018-01-01 to UTC 2024-12-31, $V = \frac{4}{3}\pi (d_{\text{max}}^3 - d_{\text{min}}^3)$ is the total comoving volume, and $(1 - \sin b_{\text{lim}})$ corrects for our Galactic latitude limit.

To maximize the statistical precision of our measurement, we combine the V -band (2014–2017) and g -band (2018–2024) samples, extending the effective survey duration to $\Delta t_{\text{tot}} = 11.0$ yr. In doing so, we use the CSP DR3 light curves (Kosciułka et al. 2017) to approximate a relation between $m_{g,\text{peak}} - m_{V,\text{peak}}$ and $M_{V,\text{peak}}$ to convert the V -band magnitudes to g -band. This method is described in Appendix D and has a scatter of 0.12 mag. While intrinsic color differences and host-galaxy extinction effects introduce systematic uncertainty at the magnitude cutoff, this effect is negligible for the rates of subtypes or between luminosity bins compared to the Poisson errors. To ensure the samples span consistent volumes, other than the different limiting apparent magnitudes ($m_{g,\text{peak}} < 17.5$ mag, $m_{V,\text{peak}} < 17.0$ mag), we apply identical constraints to both datasets: $z_{\text{min}} = 0.001$, $z_{\text{max}} = 0.08$, and a peak absolute magnitude limit of $M_{g,\text{peak}} < -16.0$ mag. The final combined rate is calcu-

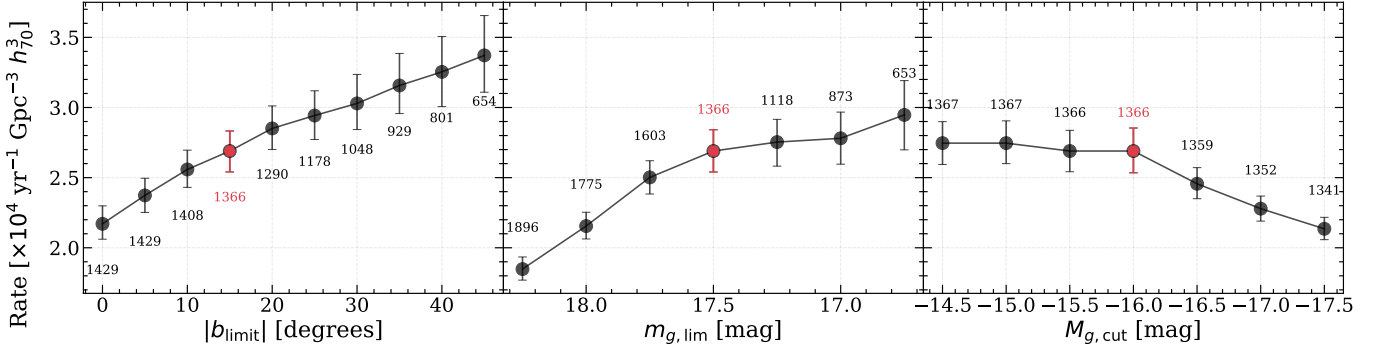


FIG. 5.— *Left*: Rate as a function of the Galactic latitude cut. *Middle*: Rate as a function of the limiting apparent magnitude. *Right*: Rate as a function of faintest peak absolute magnitude cut. In all three panels, the numbers are the number of SNe in each bin. The red points in each panel are the values used for our standard sample.

lated by summing the weights from both survey phases over the total probed volume-time:

$$R_{V+g} = \frac{\sum_{j=1}^{N_V} w_{j,V} + \sum_{i=1}^{N_g} w_{i,g}}{V \Delta t_{\text{tot}} (1 - \sin b_{\text{lim}})}, \quad (4)$$

where $w_{i,g}$ are the weights derived in this work for the $N_g = 1366$ g -band SNe, and $w_{j,V}$ are the weights derived in D24 for the $N_V = 410$ V -band SNe. By combining these datasets, we achieve the sample size necessary to robustly constrain the rates of rare subtypes where Poisson errors are the limiting factor.

4. VOLUMETRIC RATES

4.1. Total Rate

Figure 5 illustrates the sensitivity of the total volumetric rate to our primary selection criteria. We adopt a Galactic latitude cut of $|b| > 15^\circ$ to maximize the sample size while avoiding the high extinction and stellar crowding of the Galactic plane (left panel). The middle panel shows the stability of the rate as a function of the limiting apparent magnitude. The rate remains consistent within uncertainties for $m_{g,\text{lim}} \leq 17.5$ mag but declines at fainter magnitudes, suggesting that our completeness corrections are imperfectly accounting for the rapid drop in detection efficiency. Consequently, we adopt $m_{g,\text{lim}} = 17.5$ mag as the limit for the standard sample.

The choice of the absolute magnitude cut ($M_{g,\text{cut}}$) significantly impacts both the calculated rate and its precision (right panel). Extending the limit to include intrinsically faint SNe (e.g., pushing $M_{g,\text{cut}}$ from -17.0 to -15.0 mag) increases the total volumetric rate, indicating the presence of a significant low-luminosity population. However, because these events are difficult to detect, they require large completeness corrections ($w_{i,g}$). The combination of their significant contribution to the total number and their high statistical weights results in a disproportionate inflation of the uncertainty. This trade-off was also observed in the V -band analysis of Paper I (D24). To balance the inclusion of fainter populations with statistical robustness, we adopt $M_{g,\text{cut}} = -16.0$ mag for our standard sample.

For our standard g -band sample of 1366 SNe Ia ($M_{g,\text{peak}} < -16.0$ mag, $m_{g,\text{peak}} < 17.5$ mag, $|b| > 15^\circ$, and $0.001 < z < 0.08$), using Equation 3, we measure a

total volumetric rate of

$$R_{\text{tot},g} = (2.69 \pm 0.14) \times 10^4 \text{ yr}^{-1} \text{ Gpc}^{-3} h_{70}^3, \quad (5)$$

at a median redshift of $z_{\text{med}} = 0.03$. The fractional uncertainty of 5.2% exceeds the Poisson expectation (2.7%) due to the non-uniform weighting required to correct for completeness driven by the subset of SNe with low detection probabilities and high weights. However, thanks to the ~ 3.4 times larger sample size of the g -band survey, there is a significant improvement in precision over the V -band measurement (9% uncertainty; D24).

By combining the V - and g -band samples (Equation 4), we leverage the full statistical power of the 11-year ASAS-SN baseline. Using the 1776 SNe Ia with $M_{g,\text{peak}} < -16.0$ mag, $m_{g,\text{peak}} < 17.5$ mag, $m_{V,\text{peak}} < 17.0$ mag, $|b| > 15^\circ$, and $0.001 < z < 0.08$, we find a final ASAS-SN SN Ia rate of

$$R_{\text{tot}} = (2.55 \pm 0.12) \times 10^4 \text{ yr}^{-1} \text{ Gpc}^{-3} h_{70}^3 \quad (6)$$

at a median redshift of $z = 0.029$. With a total uncertainty of only 4.7%, this is the most precise measurement of the local volumetric SN Ia rate to date.

While we will discuss rates as a function of galaxy properties in later papers, we can rephrase Equation 6 in units roughly representing the rate in L_* galaxies like the Milky Way. The density scale of L_* galaxies is $n_* \approx 0.01 h^3 \text{ Mpc}^{-3}$ (e.g., Blanton et al. 2003; Bell et al. 2003) and $h = 0.7$, so the rate per L_* galaxy per century is approximately

$$R_{\text{tot}} n_*^{-1} = 0.74 (L_* \text{ galaxy})^{-1} \text{ century}^{-1}. \quad (7)$$

This is consistent with estimates of the SN Ia rate in the Galaxy of $1.4^{+1.4}_{-0.8} \text{ century}^{-1}$ (e.g., Adams et al. 2013). Equivalently, a rate of one SN Ia per L_* galaxy per century is $3.4 \times 10^4 \text{ yr}^{-1} \text{ Gpc}^{-3} h_{70}^3$.

Figure 6 places the total rate in the context of previous studies. When interpreting these comparisons, the differing absolute magnitude limits of each survey must be considered. While Frohmaier et al. (2019) restricted their sample to ‘cosmologically useful’ SNe Ia ($M < -18.0$ mag), Perley et al. (2020) reached -16.5 mag, and some volume-limited studies integrated as faint as -15.0 or -14.0 mag (Srivastav et al. 2022; Ma et al. 2025b). Because the SN Ia luminosity function remains relatively flat down to $M \approx -16$ mag (see Section 5), the total integrated rate is sensitive to the choice of this cutoff. Consequently, the value we report is formally the rate

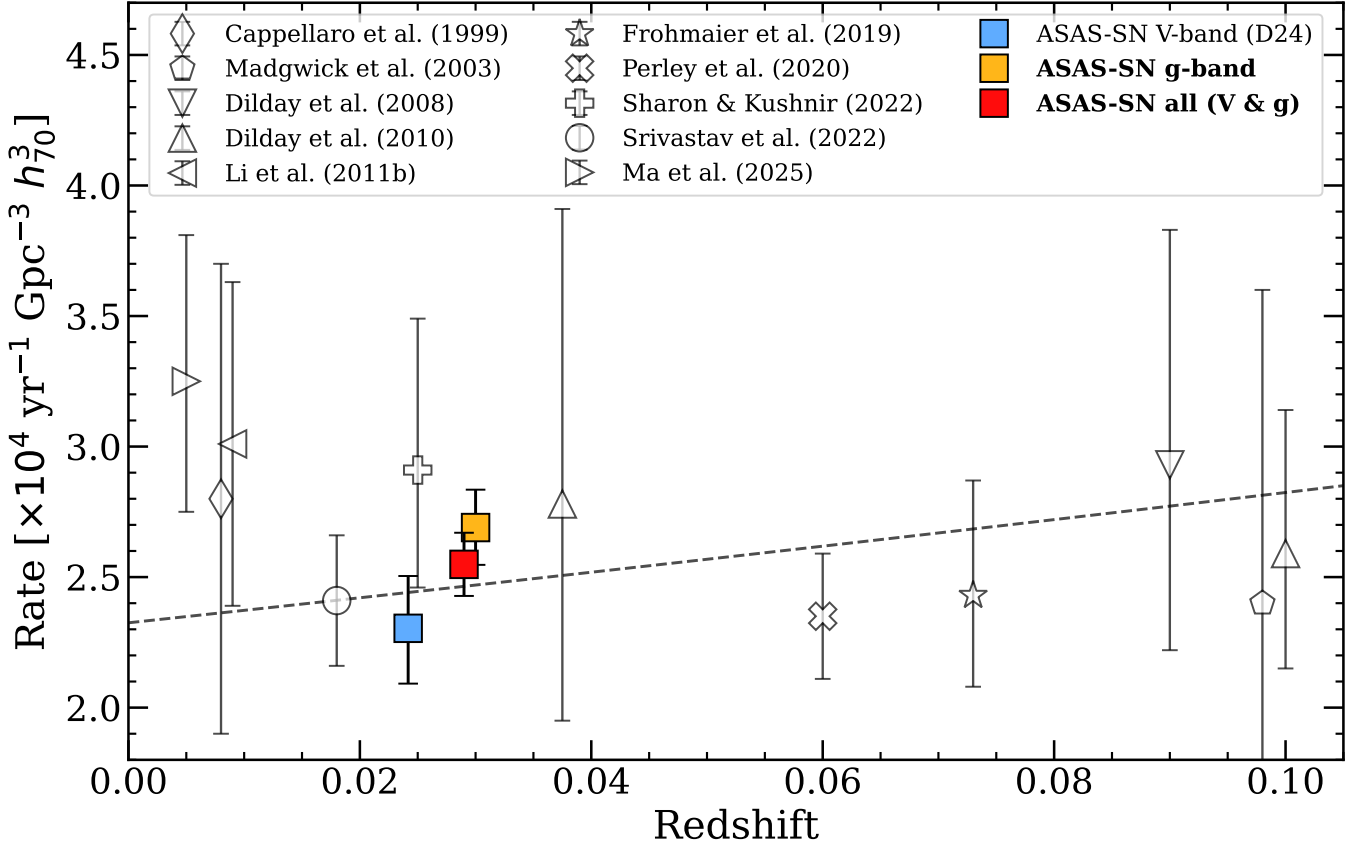


FIG. 6.— Volumetric SN Ia rate as a function of redshift z . ASAS-SN rates from V -band (D24) and g -band, separately, and the final rate from combining the entire ASAS-SN sample are shown as filled squares at the median redshift of each sample ($M_{g,\text{peak}} < -16.0$ mag). Rates from other studies are shown as open symbols (Cappellaro et al. 1999; Madgwick et al. 2003; Dilday et al. 2008, 2010; Li et al. 2011b; Frohmaier et al. 2019; Perley et al. 2020; Sharon & Kushnir 2022; Srivastav et al. 2022; Ma et al. 2025b). The dashed line shows the power-law derived by Dilday et al. (2010) for all SNe Ia (including all subtypes), scaling as $(1 + z)^\alpha$ with $\alpha = 2.04^{+0.90}_{-0.89}$.

for SNe Ia with $M_{g,\text{peak}} < -16.0$ mag, rather than the rate for all SNe that could be spectroscopically classified as SNe Ia regardless of their absolute magnitude.

With this definition, our rate from Equation 6 is statistically consistent with measurements from other untargeted surveys. These include PTF ($(2.43 \pm 0.29) \times 10^4 \text{ yr}^{-1} \text{ Gpc}^{-3} h_70^3$; Frohmaier et al. 2019), the ZTF Bright Transient Survey ($(2.35 \pm 0.24) \times 10^4 \text{ yr}^{-1} \text{ Gpc}^{-3} h_70^3$; Perley et al. 2020), and ATLAS ($(2.41 \pm 0.25) \times 10^4 \text{ yr}^{-1} \text{ Gpc}^{-3} h_70^3$; Srivastav et al. 2022). The volume-limited ZTF rate from Sharon & Kushnir (2022) is slightly higher, although statistically consistent; their analysis includes a correction for host-galaxy extinction, which will increase the estimated rate. While broadly consistent with these studies, the ASAS-SN measurement benefits from reduced systematic uncertainties. Unlike previous efforts, we explicitly model the survey completeness as a function of both peak absolute magnitude and light-curve shape, and over observing seasons, using subtype-specific templates to accurately characterize the selection function across the full diversity of the SN Ia population, down to the faintest luminosities.

In contrast, our rate is lower than estimates from older galaxy-targeted surveys (e.g., Cappellaro et al. 1999; Li et al. 2011b), though the large uncertainties in those works maintain statistical consistency. We ob-

serve a mild tension with the recent measurement of $3.25^{+0.56}_{-0.50} \times 10^4 \text{ yr}^{-1} \text{ Gpc}^{-3} h_70^3$ by Ma et al. (2025b); this likely stems from cosmic variance within their smaller volume ($D < 40 \text{ Mpc}$) and methodological differences between characterizing the selection function of a heterogeneous compilation versus a single, uniform survey. Finally, our local rate measurement agrees with the expected $(1 + z)^\alpha$ evolution derived from higher-redshift samples (e.g., Dilday et al. 2010).

4.2. Subtype Rates

A primary motivation for this work is to leverage the statistical power of the combined 11-year ASAS-SN sample to robustly measure the volumetric rates of SN Ia subtypes. These rates and fractions are presented in Table 3.

The “Ia-norm+other” category, which includes normal SNe Ia, transitional events, subluminous 91bg-like events, and SNe lacking a specific subtype classification, dominates the population, accounting for $(92.7 \pm 1.9)\%$ of the total rate in our standard sample. While we broadly categorize 91bg-like events as part of the normal distribution, we estimate a lower limit of $R_{91\text{bg}} \geq (1.7 \pm 0.4) \times 10^3 \text{ yr}^{-1} \text{ Gpc}^{-3} h_70^3$ ($\geq 6.7\%$ of total SN Ia rate) for the rate of this specific spectroscopic subclass using only those events explicitly classified as 91bg-like on TNS. This estimate is notably lower than the

TABLE 3

Volumetric rates and relative fractions for SN Ia subtypes using the combined $V+g$ dataset. The primary rows show the standard sample ($M_{g,\text{peak}} < -16.0$ mag). Rows in italics show the values for the fainter absolute magnitude cut ($M_{g,\text{peak}} < -15.0$ mag) where they differ; values not listed remain unchanged. All fractions are relative to the total rate for the specific sample.

Subtype	N	Rate [$\text{yr}^{-1} \text{Gpc}^{-3} h_{70}^3$]	Fraction [%]
Ia-norm+other	1642	$(2.36 \pm 0.11) \times 10^4$	92.7 ± 1.9
<i>($M < -15$)</i>	<i>–</i>	<i>–</i>	<i>91.4 ± 1.7</i>
Iax	9	800 ± 400	3.0 ± 1.4
<i>($M < -15$)</i>	<i>10</i>	<i>$(1.1 \pm 0.5) \times 10^3$</i>	<i>4.3 ± 1.8</i>
Ia-91T	108	850 ± 100	3.3 ± 0.4
Ia-02es	4	210 ± 130	0.8 ± 0.5
Ia-03fg	8	32 ± 12	0.12 ± 0.05
Ia-CSM	5	9 ± 4	0.036 ± 0.017
Total	1776	$(2.55 \pm 0.12) \times 10^4$	100
<i>($M < -15$)</i>	<i>1777</i>	<i>$(2.58 \pm 0.12) \times 10^4$</i>	<i>100</i>

$\sim 15 - 16\%$ fractions reported by previous studies (Li et al. 2011a; Ma et al. 2025a). However it is inherently a lower limit, as it is restricted to SNe with spectra of sufficient quality showing a strong Ti II absorption feature; additional candidates likely remain hidden within the Ia-norm+other population. It is also likely that the galaxy-targeted strategy of the LOSS sample (Li et al. 2011a) inherently biases the 91bg-like rate because it focused on more massive hosts, and fast-declining, 91bg-like SNe are preferentially found in massive early-type galaxies (e.g., Hamuy et al. 2000; Neill et al. 2009; Barkhudaryan et al. 2019; Rigault et al. 2020).

With 108 91T-like SNe observed in our standard sample, we measure a volumetric rate of $R_{91T} = (850 \pm 100) \text{ yr}^{-1} \text{ Gpc}^{-3} h_{70}^3$ ($3.3 \pm 0.4\%$). With a more precise measurement, our observed fraction for this subtype is still consistent with the V -band analysis in Paper I (4%; D24) and the $5.4_{-3.8}^{+3.6}\%$ fraction found in the recent compilation by Ma et al. (2025a). It is also statistically consistent (1.5σ) with the higher fraction of $9.4_{-4.7}^{+5.9}\%$ reported for the volume-limited LOSS sample (Li et al. 2011a), owing to their large uncertainties.

We find that SNe Iax (02cx-like) comprise $(3.0 \pm 1.4)\%$ of the total rate in our standard sample ($M_{g,\text{peak}} < -16.0$ mag). Extending the limit to $M_{g,\text{peak}} < -15.0$ mag adds one SN Iax to the sample (and no other subtypes), raising the Iax fraction to $(4.3 \pm 1.8)\%$ and marginally increasing the total SN Ia volumetric rate to $R_{\text{tot}} = (2.58 \pm 0.12) \times 10^4 \text{ yr}^{-1} \text{ Gpc}^{-3} h_{70}^3$. These fractions are consistent with the $5.4_{-3.3}^{+4.7}\%$ and $6.8_{-3.4}^{+4.0}\%$ reported by Li et al. (2011a) and Ma et al. (2025a), respectively. Our results are also statistically consistent with the higher fraction of $15_{-9}^{+17}\%$ estimated by Srivastav et al. (2022) using a volume-limited sample from ATLAS. While the uncertainties on their measurements are large, Srivastav et al. (2022) find that the Iax population is dominated by low-luminosity events ($M \gtrsim -16$ mag), which alone account for $\sim 12\%$ of the total SN Ia rate in their analysis. Because these subluminous events largely fall below our standard absolute magnitude cut ($M < -16$ mag) and

sensitivity limits, our measured rate likely represents a lower bound. If the Iax LF does not turnover rapidly at $M_{g,\text{peak}} > -15.0$ mag, these faint explosions could contribute significantly more to the total SN Ia volumetric rate.

The rarest subtype are the SNe showing interaction with circumstellar material (CSM). We find a rate for SNe Ia-CSM of $R_{\text{Ia-CSM}} = (9 \pm 4) \text{ yr}^{-1} \text{ Gpc}^{-3} h_{70}^3$, corresponding to only $(0.036 \pm 0.017)\%$ of the total SN Ia rate. This rate is consistent with the V -band measurement of $R_{\text{Ia-CSM}} = 10 \pm 7 \text{ yr}^{-1} \text{ Gpc}^{-3} h_{70}^3$ (D24) and with the low fractions ($0.02 - 0.2\%$) found in the ZTF Bright Transient Survey (Sharma et al. 2023), but much better constrained. The presence of dense, hydrogen-rich CSM has been attributed to various progenitor scenarios, such as mergers within a common envelope or winds from non-degenerate companions; however, the specific mechanism required to produce the often massive CSM inferred for these events remains debated (e.g., Hamuy et al. 2003; Livio & Riess 2003; Lundqvist et al. 2013; Meng & Podsiadlowski 2017). Regardless of the exact progenitor channel(s), our measurement confirms the extreme rarity of these SNe Ia-CSM, a conclusion reinforced by the strict limits on late-time CSM interaction derived from ultraviolet observations (e.g., Graham et al. 2019; Dubay et al. 2022). This provides strong demographic evidence that this specific evolutionary pathway contributes less than 0.05% to the total population of thermonuclear explosions in the local universe.

We provide new constraints on the rates of two of the most peculiar and physically enigmatic SN Ia subtypes: the subluminous 02es-like and the luminous 03fg-like SNe. We find $R_{02es} = (210 \pm 130) \text{ yr}^{-1} \text{ Gpc}^{-3} h_{70}^3$ and $R_{03fg} = (32 \pm 12) \text{ yr}^{-1} \text{ Gpc}^{-3} h_{70}^3$. While the 03fg-like rate is consistent with the V -band measurement from Paper I, the rate for 02es-like events is marginally higher. This increase is likely driven by the g -band survey’s deeper limiting magnitude ($g \lesssim 17.5$ mag vs $V \lesssim 17.0$ mag), allowing a lower-luminosity limit, and improved spectroscopic classification efficiency for these rare events.

These two subtypes have recently been linked observationally. Hoogendam et al. (2024) showed that 02es-like and 03fg-like SNe are the *only* subtypes to exhibit non-monotonic bumps in their rising light curves (e.g., Cao et al. 2015; Miller et al. 2020; Burke et al. 2021; Jiang et al. 2021; Srivastav et al. 2023; Dimitriadis et al. 2023; Abreu Paniagua et al. 2025). Based on these shared properties, recent studies have theorized that these events might represent different ends of a physical continuum, perhaps defined by progenitor core mass (e.g., Ashall et al. 2021; Hoogendam et al. 2024). Regardless of the specific physical driver, our rates provide constraints on such scenarios.

We find that 02es-like SNe are significantly more common than 03fg-like SNe, with a rate ratio of $R_{02es}/R_{03fg} = 7 \pm 5$. Since 02es-like events are faint and extend to the faintest absolute magnitudes, this ratio is really a lower limit. If these subtypes indeed form a continuum, the underlying progenitor channel must strongly favor the production of lower-luminosity explosions. This provides a demographic constraint for progenitor models, such as violent white dwarf mergers (e.g., Pakmor et al.

2010; Kromer et al. 2016) or core-degenerate scenarios (e.g., Kashi & Soker 2011; Ashall et al. 2021), that attempt to explain their shared properties of a C-rich envelope and unusual rising light curves (Hoogendam et al. 2024).

5. LUMINOSITY FUNCTIONS

We construct the luminosity functions (LFs) for SNe Ia and their subtypes by leveraging the full statistical power of the combined $V+g$ ASAS-SN dataset. This 11-year baseline enables the most detailed demographic study of SN Ia subtypes in the local universe to date. The resulting LFs, corrected only for Galactic extinction, are presented in Figure 7.

Following the methodology of D24, we divide the SNe in our combined sample (Section 2) into 0.5 mag bins and calculate the differential volumetric rate using Equation 4. For the two least luminous and the one most luminous magnitude bins containing no detected events, we calculate upper limits using a Monte Carlo approach. We simulate 10^5 artificial sources uniformly distributed in comoving volume and magnitude within the bin limits. By convolving these simulated sources with our survey completeness function, we determine the mean detection probability and the resulting effective survey volume. The reported limits correspond to the volumetric rate that would yield a Poisson expectation of 1.15 detected events (1σ confidence) given this effective volume-time product.

The total SN Ia LF (red squares in Figure 7) exhibits the characteristic shape observed in previous studies, peaking at $M_{g,\text{peak}} \approx -19$ mag. Figure 7 compares our results to the V -band-only LF from Paper I (D24) and the ZTF r -band LF from Perley et al. (2020). For a direct comparison, we transformed these distributions into the g band following the method detailed in Appendix D; this procedure applies the necessary offsets to the absolute magnitudes and scales the rates to account for differences in bin width. The results are broadly consistent within the uncertainties across the full luminosity range, though our g -band and combined LFs extend to lower luminosities. While the data suggest a downturn faintward of $M_{g,\text{peak}} \approx -16$ mag, we note that the faintest bin contains only a single SN and is heavily reliant on volume corrections. Nevertheless, the LF must eventually turn over.

We briefly consider the implications for host-galaxy extinction similar to Paper I (D24). The agreement between the g - and V -band LFs, with no discernible magnitude offset, is likely due to the significant overlap in their filter response functions. By comparing these distributions to the ZTF r -band LF from Perley et al. (2020), we estimate a mean host extinction of $E(V-r)_{\text{host}} \approx E(g-r)_{\text{host}} \approx 0.2$ mag. It is important to note, however, that this value does not account for very highly extinguished SNe that are largely excluded from magnitude-limited optical surveys.

Figure 8 presents the subtype-specific LFs with the data and upper limits given in an ancillary file. To provide physical context, the right axis shows the rate normalized to that for L_* (Milky Way-like) galaxy per century, as done for Equation 7.

The luminosity function of 91T-like SNe exhibits a spread of ~ 2 mag. This broad distribution is consis-

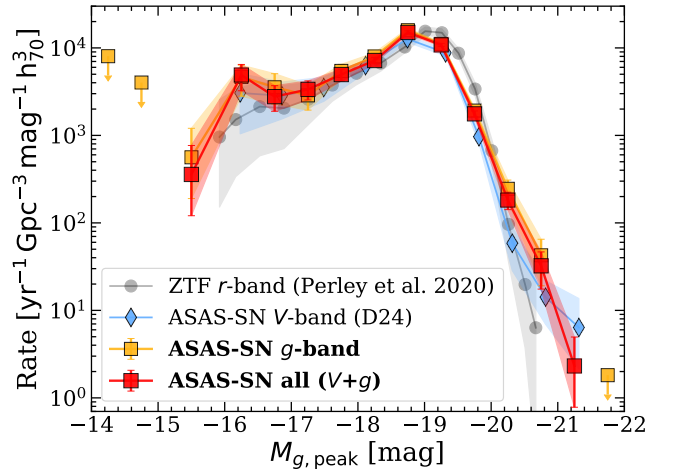


FIG. 7.— Comparison of the total SN Ia luminosity functions derived from the combined ASAS-SN $V+g$ sample (red squares) and g -band only sample (golden squares) with the V -band LF from Paper I (blue diamonds; D24) and the ZTF r -band LF from Perley et al. (2020) (grey circles). The combined sample provides tighter constraints, particularly at the faint end.

tent with the preference of 91T-like SNe for star-forming host galaxies (e.g., Howell 2001; Sullivan et al. 2010; Phillips et al. 2024), where the progenitors are often subject to significant host-galaxy extinction of up to $E(B-V)_{\text{host}} \approx 0.4$ mag (Phillips et al. 2022). Additionally, the likely inclusion of 99aa-like and shallow-silicon events contributes to the width of the 91T-like distribution, as these subtypes are intrinsically fainter than pure 91T-like events (e.g., Phillips et al. 2022).

The SNe Iax LF is notably broad, spanning nearly five magnitudes from $M_{g,\text{peak}} \approx -20$ mag and rising towards our faint limit of -15 mag. This diversity aligns with recent evidence suggesting that SNe Iax comprise two distinct populations based on absolute magnitude and decline rates: a luminous group ($M_{\text{peak}} \lesssim -16$ mag) and a low-luminosity group ($M_{\text{peak}} \gtrsim -16$ mag) (e.g., Magee et al. 2016; Srivastav et al. 2022; Singh et al. 2023). The low-luminosity population includes some extremely faint events such as SNe 2008ha, 2010ae, 2019gsc, 2020kyg, and 2021fcg, all with $M_{\text{peak}} > -15$ mag (Foley et al. 2009; Stritzinger et al. 2014; Srivastav et al. 2020, 2022; Karambelkar et al. 2021). While our measured Iax fraction ($4.3 \pm 1.8\%$) is statistically consistent with volume-limited estimates (Li et al. 2011a; Srivastav et al. 2022; Ma et al. 2025a), the rising LF suggests we may be missing a significant low-luminosity tail of the distribution. Srivastav et al. (2022) estimate that a significant fraction of SNe Iax are fainter than $M_{\text{peak}} = -16$ mag; given that many of these events fall below our magnitude cut, the true intrinsic rate of SNe Iax is likely higher. This luminosity distribution is consistent with pure deflagration models of Chandrasekhar-mass WDs, which predict a diverse range of outcomes from weak partial deflagrations to near-complete disruptions (Fink et al. 2014; Jha 2017).

Finally, we provide the first robust LFs for the peculiar 02es-like and 03fg-like subtypes from a systematic survey. The 03fg-like LF spans $M_{\text{peak}} \approx -20.5$ to -18.5 mag, whereas the 02es-like LF occupies a distinctly fainter regime from $M_{\text{peak}} \approx -18.5$ down to -16.5 mag. When

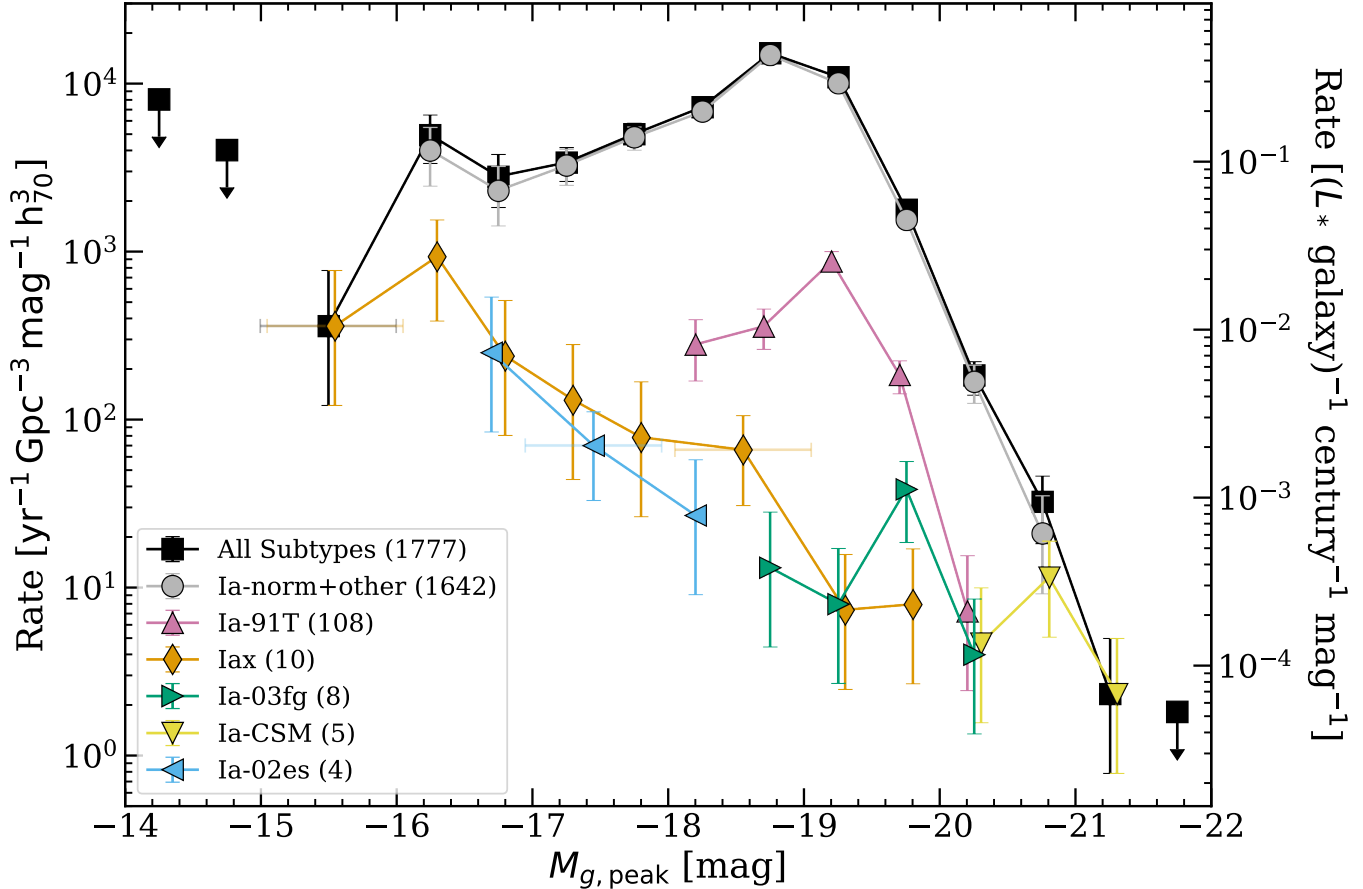


FIG. 8.— The g -band luminosity functions (LF) for SN Ia subtypes derived from the combined ASAS-SN V - and g -band samples. The total LF is shown in black, while LFs for individual subtypes are color-coded as indicated in the legend (sample sizes in parentheses). The points with downward arrows are 1σ upper limits. For clarity, the bin centers for SN Ia-91T and SN Ia-02es are shifted by $+0.05$ mag, and those for SN Iax and SN Ia-CSM by -0.05 mag. The standard bin width is 0.5 mag and the bins marked with horizontal bars have a width of 1.0 mag. The right axis shows the rate normalized to an L_* galaxy per century per mag assuming $n_* = 0.01 h^3 \text{ Mpc}^{-3}$ (e.g., Blanton et al. 2003; Bell et al. 2003). The tabulated data for these LFs, including the upper limits for all subtypes, are available in the ancillary materials.

viewed together, these subtypes populate a continuous range of luminosities divided roughly at $M_{\text{peak}} \approx -18.5$ mag. This observed luminosity continuum is consistent with theoretical frameworks where these subtypes arise from a single progenitor channel governed by a physical parameter, such as core mass (e.g., Ashall et al. 2021; Hoogendoorn et al. 2024). The difference in peak magnitude likely correlates with effective temperature, naturally explaining the spectroscopic differences between the cooler, Ti II-rich 02es-like events and the hotter 03fg-like events. Furthermore, the combined 02es-like and 03fg-like LF is heavily skewed towards the faint end, reinforcing the implication that any common progenitor channel must strongly favor lower-luminosity explosions. Additionally, if the 02es-like LF continues to rise faintward of $M_{g,\text{peak}} = -16.5$ mag, similar to the behavior discussed for SNe Iax, then our reported rate represents only a lower bound on a potentially much larger population of low-luminosity transients.

6. SUMMARY & CONCLUSION

In this third study of SN rates in ASAS-SN, we have analyzed the combined 11-year sample of SNe Ia discovered and recovered by ASAS-SN between 2014 and 2024.

By integrating the high spectroscopic completeness of the V -band era (Paper I; D24) with the depth and statistics of the g -band era, we provide the most statistically rigorous benchmark for the local SN Ia population to date. Our main conclusions are as follows:

- We measure a total volumetric SN Ia rate for our standard sample ($M_{g,\text{peak}} < -16.0$ mag) of $R_{\text{tot}} = (2.55 \pm 0.12) \times 10^4 \text{ yr}^{-1} \text{ Gpc}^{-3} h_70^3$. This result is consistent with previous untargeted surveys (e.g., Frohmaier et al. 2019; Perley et al. 2020; Srivastav et al. 2022) but offers a significant improvement in precision (4.7% total uncertainty) due to the extended baseline and uniform selection function of ASAS-SN. This measurement serves as a robust anchor for determining the redshift evolution of the SN Ia rate.
- We provide robust volumetric rates for the SN Ia subtypes. The “Ia-norm+other” category dominates, accounting for $(92.7 \pm 1.9)\%$ of the total rate. For the luminous 91T-like SNe, we measure a rate of $(850 \pm 100) \text{ yr}^{-1} \text{ Gpc}^{-3} h_70^3$ ($3.3 \pm 0.4\%$ of the total). SNe Iax have a rate of $(4.3 \pm 1.8)\%$ of the total rate when considering SNe down to

$M_{g,\text{peak}} < -15.0$ mag. However, because the SNe Iax LF rises toward lower luminosity, this value likely represents a lower bound on their true population.

- We find that the subluminous 02es-like SNe ($210 \pm 130 \text{ yr}^{-1} \text{ Gpc}^{-3} h_{70}^3$) are significantly more common than the luminous 03fg-like SNe ($32 \pm 12 \text{ yr}^{-1} \text{ Gpc}^{-3} h_{70}^3$). The ratio of their rates is $R_{02\text{es}}/R_{03\text{fg}} = 7 \pm 5$. This large ratio and their LFs place strong demographic constraints on theoretical models that propose a physical continuum for these two subtypes (e.g., [Ashall et al. 2021](#); [Hoogendam et al. 2024](#)), implying that any common progenitor channel must strongly favor the production of lower-luminosity explosions. If there are any undetected or unclassified 02es-like SNe below $M_{g,\text{peak}} = -16.5$ mag, then the true volumetric rate of these events will be higher than measured here.
- We confirm the extreme rarity of SNe Ia-CSM associated with dense circumstellar material. We measure a rate for SNe Ia-CSM of $(9 \pm 4) \text{ yr}^{-1} \text{ Gpc}^{-3} h_{70}^3$, corresponding to only $(0.036 \pm 0.017)\%$ of the total SNe Ia rate. This implies that the evolutionary pathways producing massive CSM shells around SN Ia progenitors are exceptionally rare in the local universe.
- The combined luminosity functions reveal immense diversity in the SNe Ia population. SNe Ia-CSM appear only in the most luminous bins. The 02es-like and 03fg-like subtypes occupy distinct luminosity ranges that together form a potential continuum. The SNe Iax distribution is extremely broad, extending from $M_{g,\text{peak}} \approx -20$ mag down to the limit of -15.0 mag.

The total SN Ia LF is broad and spans more than five magnitudes. This has significant implications for the physical parameters of the explosions. If the peak luminosity simply scales linearly with the mass of synthesized radioactive nickel ($L_{\text{peak}} \propto M_{56\text{Ni}}$; [Arnett 1982](#)), this implies that the nickel yields of SNe Ia vary by a factor of nearly 100. This range is significantly larger than the factor of ~ 10 typically invoked in theoretical models (e.g., [Piro et al. 2014](#)). Furthermore, to the extent that nickel mass correlates with the total kinetic energy of the explosion, the resulting SN remnants must originate from events spanning two orders of magnitude in energy.

Finally, we discuss the low-luminosity end of the LF. While the total LF shows a tentative downturn fainter

than $M_{g,\text{peak}} \approx -16$ mag, we find no statistical evidence for a decline in the rates of subluminous subtypes, such as SNe Iax and 02es-like SNe. The true contribution of these low-luminosity transients depends heavily on the behavior of the LF beyond our current limits. We consider three scenarios. First, if the rate declines rapidly, our current measurements of the SN Ia rate and subtype fractions are robust. Second, if the LF remains flat at $\approx 10^3 \text{ yr}^{-1} \text{ Gpc}^{-3} \text{ mag}^{-1}$ past -16 mag, the population would need to extend down to 9 mag to account for 50% of the total SN Ia rate, and down to -3 mag to account for 25%. This would be nonphysical for SNe. Third, if the rate continues to rise with the slope observed for SNe Iax ($\log_{10}(R_{\text{Iax}}) \propto 0.475 M_{g,\text{peak}}$) these events could be more abundant than their higher-luminosity counterparts, reaching 50% of the total rate if such a trend extends to ~ -12.5 mag. A SN at -12.5 mag is only detectable within 10 Mpc for ASAS-SN's 17.5 mag limit. We likely underestimate the abundance of these low-luminosity events because candidates are frequently recognized as intrinsically faint only post-peak, bypassing triggers designed for studying rising, normal SNe Ia. To fully characterize the physics of thermonuclear explosions, we encourage time-domain surveys with deeper limiting magnitudes to prioritize the nearby volume, specifically targeting transients fainter than -16 mag to constrain this faint population.

The next paper in this series will extend this 11-year analysis to the core-collapse supernova population. Subsequent work will then leverage these combined subtype-specific samples to determine rates as a function of host-galaxy properties. By isolating the environmental dependencies of distinct populations, we aim to map specific evolutionary pathways to their observed outcomes. This demographic analysis is essential for establishing a physical link between the progenitor systems, their host environments, and the resulting explosion mechanisms.

ACKNOWLEDGMENTS

We thank Federica Chiti for helpful discussions.

The Shappee group at the University of Hawai‘i is supported with funds from NSF (grant AST-2407205) and NASA (grants HST-GO-17087, 80NSSC24K0521, 80NSSC24K0490, 80NSSC23K1431). CSK and KZS are supported by NSF grants AST-2307385 and AST-2407206. ASAS-SN is funded by Gordon and Betty Moore Foundation grants GBMF5490 and GBMF10501 and the Alfred P. Sloan Foundation grant G-202114192. JFB is supported by NSF grant PHY-2310018. SD is supported by the National Natural Science Foundation of China (Grant No. 12133005). JL is supported by NSF-2206523.

REFERENCES

Abreu Paniagua I. A., et al., 2025, [arXiv e-prints](#), p. [arXiv:2508.13263](#)

Adams S. M., Kochanek C. S., Beacom J. F., Vagins M. R., Stanek K. Z., 2013, [ApJ](#), **778**, 164

Arnett W. D., 1982, [ApJ](#), **253**, 785

Ashall C., et al., 2018, [MNRAS](#), **477**, 153

Ashall C., et al., 2021, [ApJ](#), **922**, 205

Ashall C., et al., 2022, [ApJ](#), **932**, L2

Astropy Collaboration et al., 2013, [A&A](#), **558**, A33

Astropy Collaboration et al., 2018, [AJ](#), **156**, 123

Barkhudaryan L. V., Hakobyan A. A., Karapetyan A. G., Mamon G. A., Kunth D., Adibekyan V., Turatto M., 2019, [MNRAS](#), **490**, 718

Bell E. F., McIntosh D. H., Katz N., Weinberg M. D., 2003, [ApJS](#), **149**, 289

Blanton M. R., et al., 2003, [ApJ](#), **592**, 819

Burke J., et al., 2021, [ApJ](#), **919**, 142

Burns C. R., et al., 2011, [AJ](#), **141**, 19

Burns C. R., et al., 2018, [ApJ](#), **869**, 56

Cao Y., et al., 2015, [Nature](#), **521**, 328

Cappellaro E., Evans R., Turatto M., 1999, [A&A](#), **351**, 459

Chen P., et al., 2022, *ApJS*, **259**, 53

Desai D. D., et al., 2024, *MNRAS*, **530**, 5016

Desai D. D., et al., 2025, *MNRAS*, **541**, 2197

Dilday B., et al., 2008, *ApJ*, **682**, 262

Dilday B., et al., 2010, *ApJ*, **713**, 1026

Dimitriadis G., et al., 2023, *MNRAS*, **521**, 1162

Dong S., et al., 2018, The Astronomer's Telegram, **12325**, 1

Dubay L. O., Tucker M. A., Do A., Shappee B. J., Anand G. S., 2022, *ApJ*, **926**, 98

Filippenko A. V., et al., 1992, *ApJ*, **384**, L15

Fink M., et al., 2014, *MNRAS*, **438**, 1762

Foley R. J., et al., 2009, *AJ*, **138**, 376

Foley R. J., et al., 2013, *ApJ*, **767**, 57

Foley R. J., Jha S. W., Pan Y.-C., Zheng W. K., Bildsten L., Filippenko A. V., Kasen D., 2016, *MNRAS*, **461**, 433

Fremling C., et al., 2020, *ApJ*, **895**, 32

Frohmaier C., et al., 2019, *MNRAS*, **486**, 2308

Gall C., et al., 2018, *A&A*, **611**, A58

Gallego-Cano E., Izzo L., Dominguez-Tagle C., Prada F., Pérez E., Khetan N., Jang I. S., 2022, *A&A*, **666**, A13

Ganeshalingam M., et al., 2012, *ApJ*, **751**, 142

Graham M. L., et al., 2019, *ApJ*, **871**, 62

Graham M. L., et al., 2022, *MNRAS*, **511**, 3682

Graur O., et al., 2023, *MNRAS*, **526**, 2977

Griffith O., et al., 2025, *arXiv e-prints*, p. arXiv:2506.19071

Hamuy M., Trager S. C., Pinto P. A., Phillips M. M., Schommer R. A., Ivanov V., Suntzeff N. B., 2000, *AJ*, **120**, 1479

Hamuy M., et al., 2003, *Nature*, **424**, 651

Hart K., et al., 2023, *arXiv e-prints*, p. arXiv:2304.03791

Hoeflich P., et al., 2021, *ApJ*, **922**, 186

Holoien T. W. S., et al., 2017a, *MNRAS*, **464**, 2672

Holoien T. W. S., et al., 2017b, *MNRAS*, **467**, 1098

Holoien T. W. S., et al., 2017c, *MNRAS*, **471**, 4966

Holoien T. W. S., et al., 2019, *MNRAS*, **484**, 1899

Hoogendam W. B., Shappee B. J., Brown P. J., Tucker M. A., Ashall C., Piro A. L., 2024, *ApJ*, **966**, 139

Hoogendam W. B., et al., 2025, *ApJ*, **988**, 209

Horiuchi S., Beacom J. F., 2010, *ApJ*, **723**, 329

Hosseinzadeh G., et al., 2017, *ApJ*, **845**, L11

Howell D. A., 2001, *ApJ*, **554**, L193

Howell D. A., et al., 2006, *Nature*, **443**, 308

Hsiao E. Y., Conley A., Howell D. A., Sullivan M., Pritchett C. J., Carlberg R. G., Nugent P. E., Phillips M. M., 2007, *ApJ*, **663**, 1187

Im M., Choi C., Yoon S.-C., Kim J.-W., Ehgamberdiev S. A., Monard L. A. G., Sung H.-I., 2015, *ApJS*, **221**, 22

Jha S. W., 2017, in Alsabti A. W., Murdin P., eds., *Handbook of Supernovae*. p. 375, doi:10.1007/978-3-319-21846-5_42

Jiang J.-a., et al., 2021, *ApJ*, **923**, L8

Karachentsev I. D., Nasonova O. G., 2013, *MNRAS*, **429**, 2677

Karambelkar V. R., et al., 2021, *ApJ*, **921**, L6

Kashi A., Soker N., 2011, *MNRAS*, **417**, 1466

Kochanek C. S., et al., 2017, *PASP*, **129**, 104502

Krisciunas K., et al., 2017, *AJ*, **154**, 211

Kromer M., et al., 2016, *MNRAS*, **459**, 4428

Li W., et al., 2011a, *MNRAS*, **412**, 1441

Li W., Chornock R., Leaman J., Filippenko A. V., Poznanski D., Wang X., Ganeshalingam M., Mannucci F., 2011b, *MNRAS*, **412**, 1473

Li L., et al., 2026, *ApJ*, **996**, 10

Livio M., Riess A. G., 2003, *ApJ*, **594**, L93

Lundqvist P., et al., 2013, *MNRAS*, **435**, 329

Ma X., et al., 2025a, *A&A*, **698**, A305

Ma X., et al., 2025b, *A&A*, **698**, A306

Madgwick D. S., Hewett P. C., Mortlock D. J., Wang L., 2003, *ApJ*, **599**, L33

Maeda K., Kuncarayakti H., Nagao T., Kawabata M., Taguchi K., Uno K., De K., 2025, *arXiv e-prints*, p. arXiv:2512.02680

Magee M. R., et al., 2016, *A&A*, **589**, A89

Maoz D., Mannucci F., 2012, *PASA*, **29**, 447

Maoz D., Sharon K., Gal-Yam A., 2010, *ApJ*, **722**, 1879

Maoz D., Mannucci F., Nelemans G., 2014, *ARA&A*, **52**, 107

Matteucci F., Recchi S., 2001, *ApJ*, **558**, 351

Meng X., Podsiadlowski P., 2017, *MNRAS*, **469**, 4763

Miller A. A., et al., 2020, *ApJ*, **898**, 56

Neill J. D., et al., 2009, *ApJ*, **707**, 1449

Neumann K. D., et al., 2023, *MNRAS*, **520**, 4356

Ni Y. Q., et al., 2022, *Nature Astronomy*, **6**, 568

Pakmor R., Kromer M., Röpke F. K., Sim S. A., Ruiter A. J., Hillebrandt W., 2010, *Nature*, **463**, 61

Parrent J. T., et al., 2016, *MNRAS*, **457**, 3702

Pasham D. R., et al., 2024, *Science Advances*, **10**, eadj8898

Perley D. A., et al., 2020, *ApJ*, **904**, 35

Pessi T., et al., 2025, *arXiv e-prints*, p. arXiv:2508.10985

Phillips M. M., Wells L. A., Suntzeff N. B., Hamuy M., Leibundgut B., Kirshner R. P., Foltz C. B., 1992, *AJ*, **103**, 1632

Phillips M. M., et al., 2022, *ApJ*, **938**, 47

Phillips M. M., et al., 2024, *ApJS*, **273**, 16

Phillips M. M., et al., 2025, *arXiv e-prints*, p. arXiv:2509.07093

Piro A. L., Thompson T. A., Kochanek C. S., 2014, *MNRAS*, **438**, 3456

Raiteri C. M., Villata M., Navarro J. F., 1996, *A&A*, **315**, 105

Riess A. G., et al., 2016, *ApJ*, **826**, 56

Rigault M., et al., 2020, *A&A*, **644**, A176

Ruiter A. J., Seitenzahl I. R., 2025, *A&A Rev.*, **33**, 1

Russell D. G., 2002, *ApJ*, **565**, 681

Sand D. J., et al., 2021, *ApJ*, **922**, 21

Schlafly E. F., Finkbeiner D. P., 2011, *ApJ*, **737**, 103

Shappee B. J., et al., 2014, *ApJ*, **788**, 48

Shappee B. J., et al., 2016, *ApJ*, **826**, 144

Sharma Y., et al., 2023, *ApJ*, **948**, 52

Sharon A., Kushnir D., 2022, *MNRAS*, **509**, 5275

Siebert M. R., et al., 2024, *ApJ*, **960**, 88

Silverman J. M., et al., 2013, *ApJS*, **207**, 3

Singh M., et al., 2023, *ApJ*, **953**, 93

Smartt S. J., et al., 2015, *A&A*, **579**, A40

Sorce J. G., Shaya E. J., 2014, *MNRAS*, **444**, 527

Srivastav S., et al., 2020, *ApJ*, **892**, L24

Srivastav S., et al., 2022, *MNRAS*, **511**, 2708

Srivastav S., et al., 2023, *ApJ*, **943**, L20

Stritzinger M. D., et al., 2014, *A&A*, **561**, A146

Sullivan M., et al., 2010, *MNRAS*, **406**, 782

Theureau G., Hanski M. O., Coudreau N., Hallet N., Martin J.-M., 2007, *A&A*, **465**, 71

Tucker M. A., et al., 2022, *PASP*, **134**, 124502

Tully R. B., Fisher J. R., 1988, *Catalog of Nearby Galaxies*

Tully R. B., et al., 2013, *AJ*, **146**, 86

Tully R. B., Courtois H. M., Sorce J. G., 2016, *AJ*, **152**, 50

White C. J., et al., 2015, *ApJ*, **799**, 52

Wyatt S. D., et al., 2021, *ApJ*, **914**, 57

Xi G., et al., 2024, *MNRAS*, **527**, 9957

Yang Y., et al., 2020, *ApJ*, **902**, 46

Yang Y., et al., 2023, *MNRAS*, **519**, 1618

Zheng W., et al., 2017, *ApJ*, **841**, 64

APPENDIX

A. LIGHT CURVE TEMPLATES

To accurately model our sample, we require templates that cover the full diversity of SN Ia morphologies. While standard stretch-based templates are sufficient for normal SNe Ia, they often fail to capture the unique evolutionary features of peculiar subtypes.

For normal (including 91bg-like and transitional) SNe Ia, we utilize the *g*-band flux templates from the Carnegie Supernova Project (CSP-II; Burns et al. 2018), accessed via SNOOPY (Burns et al. 2011). These templates, shown in the top panel of Figure A1, effectively parameterize the light curve shape using the color-stretch parameter, s_{BV} , which correlates with peak luminosity.

For the peculiar subtypes, we constructed custom templates using Gaussian Process regression on well-sampled light curves of representative objects (Figure A1, bottom panel):

- 91T-like: We combined CSP DR3 *g*-band photometry of SNe 2004gu, 2005M, 2005eq, and 2007S (Krisciunas et al. 2017) to create a master template that captures the broad, slowly declining morphology typical of this class.
- Iax: We adopted the CSP light curve of the prototype SN 2005hk (Krisciunas et al. 2017) as the fiducial template. We acknowledge, however, that this subtype likely exhibits a diversity of light curve shapes not fully captured by a single template.
- 02es-like: We generated a template from the high-

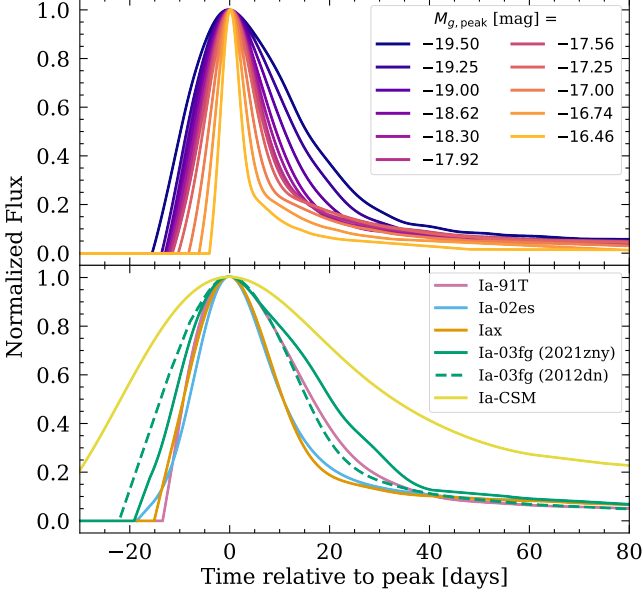


FIG. A1.— Normalized g -band flux templates, aligned at the time of maximum light ($t = 0$). *Top*: The family of templates used for normal SNe Ia. The legend indicates the peak absolute magnitude corresponding to the template shape, illustrating the stretch-luminosity relationship where brighter SNe (dark blue) are broader than fainter ones (yellow). *Bottom*: Custom templates for the subtypes. For 03fg-like SNe, we use multiple templates to capture the range of observed rise times and decline rates.

cadence ASAS-SN light curve of SN 2022vqz (Xi et al. 2024), which captures the fast evolution characteristic of this subtype.

- 03fg-like: Given the photometric diversity of this subtype, we employ two distinct templates covering the range of observed shapes: one based on SN 2012dn (Parrent et al. 2016) and another on SN 2021zny (Dimitriadis et al. 2023).
- Ia-CSM: We constructed a template using the ASAS-SN g -band light curves of SN 2018evt and SN 2022erq. These are the only two confirmed Ia-CSM events in our g -band sample, and the template exhibits the extreme width expected from interaction-powered emission.

B. DISTANCE MODULI

While redshifts provide reliable distances in the Hubble flow, the peculiar velocities of nearby galaxies introduce significant scatter. To mitigate this, we adopt redshift-independent distances for our lowest redshift events. Figure B1 compares the distance modulus derived from the redshift, $\mu(z)$, against the redshift-independent distance modulus, μ_{indep} , for the nearby SNe. The gray band illustrates the impact of a $\pm 300 \text{ km s}^{-1}$ peculiar velocity on the Hubble flow distance. As the redshift decreases, this uncertainty grows, exceeding ± 0.5 mag (red dashed lines) at approximately $\mu(z) \approx 32$ mag ($z \approx 0.006$). Therefore, for SNe with $z < 0.006$, we use redshift-independent distances from the NASA/IPAC Extragalactic Database (NED)⁴ or recent literature, when available.

⁴ <https://ned.ipac.caltech.edu/>

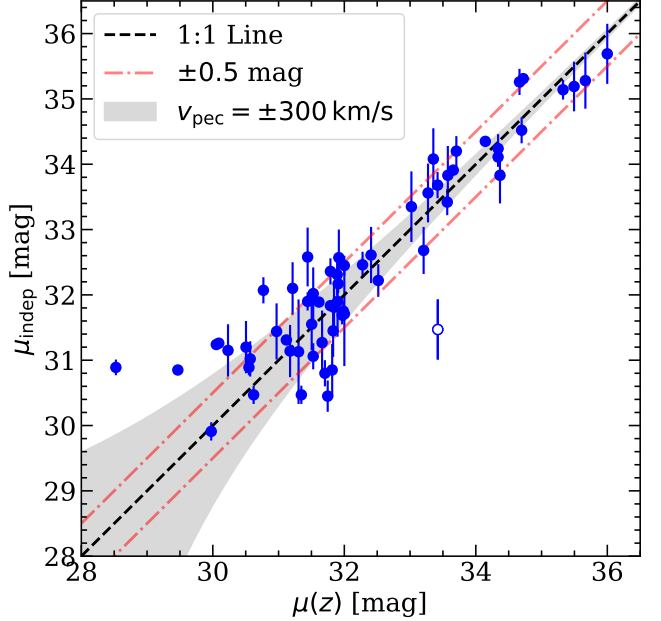


FIG. B1.— Comparison of redshift-based distance moduli ($\mu(z)$) and redshift-independent distance moduli (μ_{indep}). The solid black dashed line indicates the 1:1 relation. The gray shaded region represents the uncertainty introduced by a peculiar velocity of $v_{\text{pec}} = \pm 300 \text{ km s}^{-1}$. The red dot-dashed lines mark a ± 0.5 mag deviation, corresponding to the bin size of our luminosity functions. SN 2018fpm (open circle) is an outlier with a likely incorrect literature distance.

We list the distances and their sources in Table B1. Our search yielded redshift-independent distance moduli for 39 of the 41 SNe in this regime. One object, SN 2018fpm, deviates significantly from the 1:1 relation at $\mu(z) \approx 33.4$ mag. This discrepancy likely arises from an erroneous Tully-Fisher distance measurement in the literature (Theureau et al. 2007).

C. SPECTROSCOPIC COMPLETENESS

While the V -band survey (2014–2017) achieved a nearly spectroscopically complete sample (Holien et al. 2017a,b,c, 2019), the g -band survey (2018–2024) covers a longer baseline and reaches fainter magnitudes, resulting in a larger fraction of unclassified candidates. To incorporate these objects into our rate calculations, we include a spectroscopic completeness correction factor, F_3 . We draw our sample of unclassified candidates from the ASAS-SN discovered or recovered transients, selecting objects that satisfy three criteria: (1) a light curve morphology consistent with a supernova, (2) proximity to a potential host galaxy, and (3) the lack of a stellar counterpart in Gaia, Pan-STARRS, or TESS catalogs.

We bin both the classified SNe Ia and the unclassified candidates by year and peak apparent magnitude ($m_{g,\text{peak}}$) in 1-mag bins. We define the spectroscopic completeness as

$$F_3(y, m) = \frac{N_{\text{classified}}(y, m)}{N_{\text{total}}(y, m)}, \quad (\text{C1})$$

where $N_{\text{classified}}$ is the number of spectroscopically confirmed SNe and N_{total} is the sum of classified SNe and unclassified candidates in a given year (y) and magnitude bin (m).

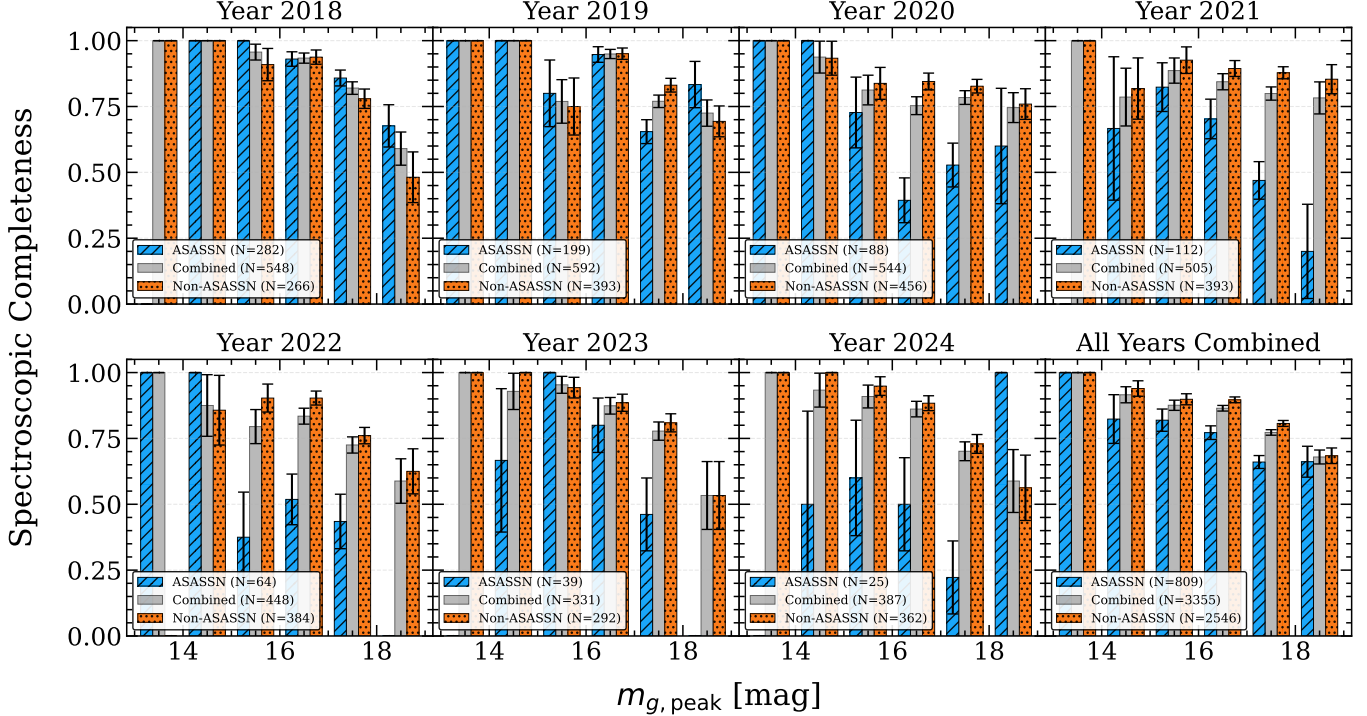


FIG. C1.— Spectroscopic completeness as a function of peak apparent g -band magnitude ($m_{g,\text{peak}}$) and year. The final panel shows the distribution for the full sample. In each plot, the completeness is shown separately for transients discovered by ASAS-SN (blue), those discovered by other surveys but recovered by ASAS-SN (orange), and the combined sample (gray). Error bars represent the binomial uncertainty in each magnitude bin.

Figure C1 presents the spectroscopic completeness as a function of peak magnitude for each year of the g -band survey. The completeness drops significantly for fainter objects ($m_{g,\text{peak}} > 17$ mag). This decline is time-dependent and stems from multiple factors. Issues following the COVID-19 pandemic disrupted classification resources starting in 2020, and as of 2022 June 1, ASAS-SN ceased soliciting confirmation images from amateur astronomers. This operational change reduced the survey’s “aggressiveness” in confirming faint or ambiguous candidates, lowering the completeness for fainter candidates in the 2022–2024 datasets compared to earlier years.

The spectroscopic incompleteness is not distributed randomly across the sky. As seen in Figure C2 the incompleteness is heavily skewed toward the Southern hemisphere ($\delta < 0^\circ$). This strong declination dependence arises from the concentration of follow-up resources in the Northern hemisphere (e.g., SCAT, Tucker et al. 2022; the ZTF Bright Transient Survey, Fremling et al. 2020; Perley et al. 2020). While major classification efforts such as ePESSTO+ (Smartt et al. 2015) and SCAT South (only since 2023; Tucker et al. 2022) target the Southern sky, their combined coverage remains significantly lower than the resources available in the North.

We apply this correction to our rate calculation by introducing the weight $F_{3,i}$ in Equation 3. This assumes that the intrinsic subtype distribution of unclassified SNe within a specific magnitude bin is the same as that of classified SNe. The strong declination dependence of our incompleteness supports the validity of this assumption: the selection function is dominated by telescope visibility limits rather than the physical properties of the super-

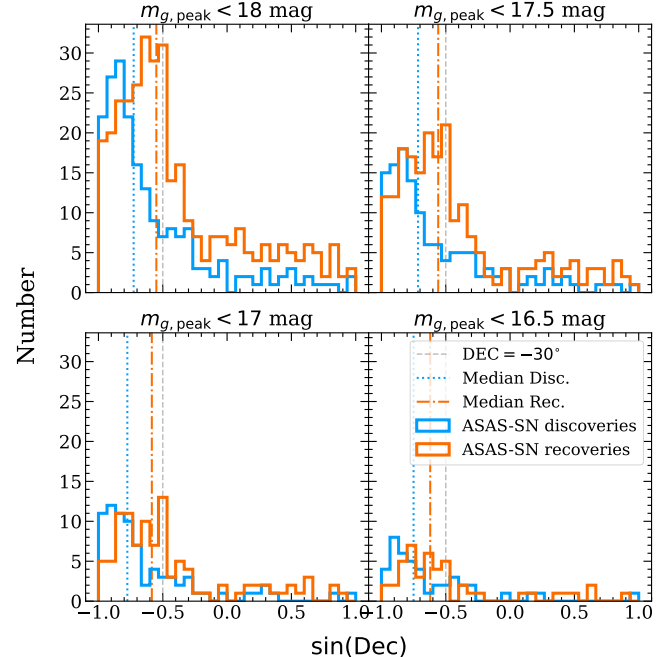


FIG. C2.— Declination distribution of unclassified transient candidates in the ASAS-SN g -band sample for peak magnitude cuts $m_g < 18.0, 17.5, 17.0, 16.5$. The histograms are binned linearly in $\sin \delta$, corresponding to bins of constant sky area. Candidates discovered by ASAS-SN are in blue and those discovered by other surveys but recovered by ASAS-SN are in orange. Vertical dotted lines indicate the median declination for each subsample. The vertical dashed gray line marks $\delta = -30^\circ$, roughly the southern limit for many major Northern hemisphere follow-up facilities. The significant skew toward negative declinations highlights the lower spectroscopic completeness in the Southern hemisphere.

TABLE B1
Redshift-independent distance moduli for $z < 0.006$ sample

SN Name	Type	z	μ_{indep} [mag]	Source
2024gy	Ia	0.0012	30.89	Li et al. (2026)
2021qvv	91bg-like	0.0018	30.85	Graur et al. (2023)
2020ukx	Ia	0.0023	29.91	Tully et al. (2013)
2021J	Ia	0.0024	31.24	Gallego-Cano et al. (2022)
2020nlb	Ia	0.0024	31.26	Sand et al. (2021)
2020req	Ia	0.0026	31.15	Tully & Fisher (1988)
2020nvb	Ia	0.0029	31.20	Tully & Fisher (1988)
2020ue	Ia	0.0030	30.89	Tully et al. (2013)
2022pul	03fg-like	0.0030	31.02	Siebert et al. (2024)
2018pv	Ia	0.0031	30.47	Tully et al. (2013)
2021hiz	Ia	0.0033	32.07	Tully et al. (2013)
2020qxp	02es-like	0.0036	31.44	Hoeflich et al. (2021)
2021pit	Ia	0.0039	31.31	Riess et al. (2016)
2017cbv	Ia	0.0040	31.14	Hosseinzadeh et al. (2017)
2015bp	91bg-like	0.0041	32.10	Wyatt et al. (2021)
2021smj	Ia	0.0042	31.13	Tully & Fisher (1988)
2018imd	Ia	0.0043	30.47	Tully et al. (2013)
ASASSN-14gh	Ia	0.0044
2024inv	Ia	0.0045
2019np	Ia	0.0045	32.58	Tully et al. (2016)
2016coj	Ia	0.0045	31.90	Zheng et al. (2017)
2024muv	Ia	0.0046	31.55	Karachentsev & Nasonova (2013)
2022hrs	Ia	0.0047	31.06	Tully et al. (2013)
2023zgx	Iax	0.0047	32.02	Tully & Fisher (1988)
2015F	Ia	0.0049	31.89	Im et al. (2015)
2021aefx	Ia	0.0050	31.27	Ashall et al. (2022)
ASASSN-14lp	Ia	0.0051	30.80	Shappee et al. (2016)
2014dt	Iax	0.0052	30.45	Foley et al. (2016)
2024xal	Ia	0.0053	32.36	Tully et al. (2013)
2018gv	Ia	0.0053	31.84	Yang et al. (2020)
2017bzc	Ia	0.0054	30.85	Russell (2002)
2017fzw	91bg-like	0.0054	31.45	Graham et al. (2022)
2023vyl	Ia	0.0054	31.81	Tully & Fisher (1988)
2017drh	Ia	0.0056	32.31	Hoogendoorn et al. (2025)
M OT J1149*	Ia	0.0056	31.90	Tully et al. (2016)
2014bv	Ia	0.0056	32.17	Tully et al. (2013)
2017igf	Ia	0.0056	32.57	Sorce et al. (2014)
2022ffv	Ia	0.0058	31.69	Tully et al. (2013)
2018aoz	Ia	0.0058	31.75	Ni et al. (2022)
2020hvf	03fg-like	0.0058	32.45	Jiang et al. (2021)
ASASSN-15us	02es-like	0.0058	31.71	Tully & Fisher (1988)

NOTE. — *Full name: MASTER OT J114925.48-050713.8.

novae. Therefore, the unobserved sample in the South is likely a random draw from the underlying spectroscopic population, avoiding any biases associated with targeting decisions based on light curve morphology or host galaxy properties.

While our magnitude-dependent correction statistically accounts for these candidates in the corresponding magnitude bins, this disparity underscores the need for increased spectroscopic follow-up resources in the Southern hemisphere to reduce the need for such statistical corrections in future surveys.

D. CONVERSION TO g -BAND

To integrate the V -band sample from our earlier ASAS-SN analyses with our current g -band sample, and to compare our results with the r -band LF from [Perley et al. \(2020\)](#), we require a method to convert peak magnitudes between these filters. Since ASAS-SN obtains single-band light curves, we cannot derive colors directly from our data. Furthermore, because SNe Ia peak at different epochs in different filters but LFs are done in terms of peak magnitude, we calculate the difference in peak magnitudes (e.g., $m_{g,\text{peak}} - m_{V,\text{peak}}$) rather than

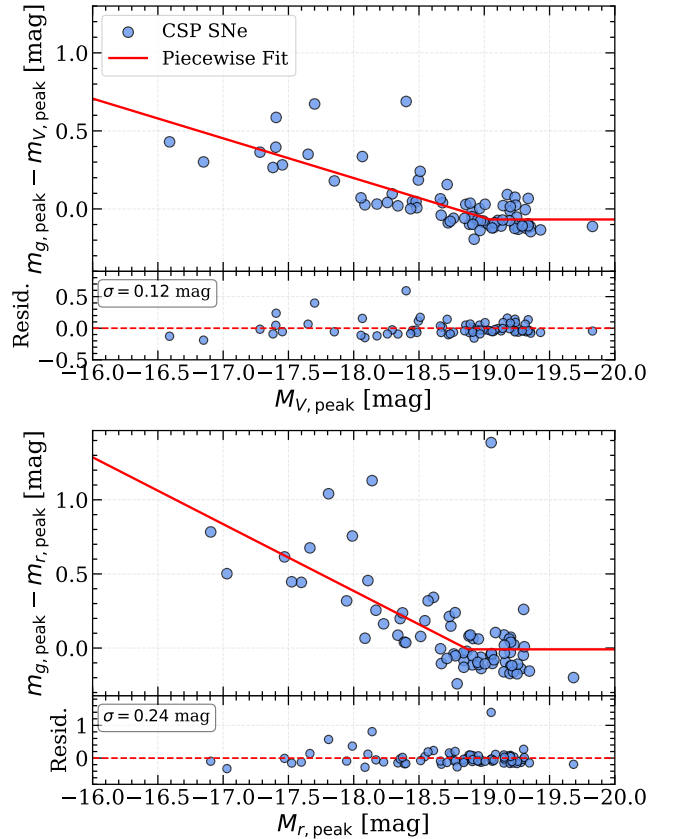


FIG. D1.— Empirical magnitude transformations derived from the CSP DR3 sample ([Krisciunas et al. 2017](#)). The blue points represent individual SNe Ia from the CSP DR3 dataset, processed with Gaussian Process fits and corrected for Milky Way extinction and K -corrections (but not host extinction). The solid red lines indicate the piecewise linear fits used to convert V and r -band peak magnitudes to the g -band.

a standard color. We derived empirical transformations for these quantities using multiband photometry from CSP DR3 ([Krisciunas et al. 2017](#)).

We constructed a set of 76 SNe Ia from CSP DR3 with well-sampled g -, r -, and V -band light curves. For each SN, we determined the peak apparent and absolute magnitudes in each filter by fitting the light curves with Gaussian Processes. To ensure consistency with our ASAS-SN sample, we corrected the CSP photometry for Milky Way extinction and K -corrections, but we did not apply corrections for host-galaxy extinction. This approach preserves the intrinsic scatter due to host reddening that is present in our ASAS-SN dataset which also does not correct for host reddening.

Figure D1 shows the relationship of the peak magnitude differences ($m_{g,\text{peak}} - m_{V,\text{peak}}$ and $m_{g,\text{peak}} - m_{r,\text{peak}}$) against the peak absolute magnitudes ($M_{V,\text{peak}}$ and $M_{r,\text{peak}}$). Bright, standardizable SNe Ia exhibit a relatively constant difference between peak magnitudes, while lower-luminosity events show a trend toward larger, redder differences.

To model this behavior, we fit a simple piecewise linear function to the data. The model is constrained to be constant for luminous SNe and increases linearly towards lower luminosities. The resulting relations for the V and

r bands are given by

$$\Delta m_{gV} = \begin{cases} -0.067, & M_V < -19.042 \\ -0.067 + 0.255(M_V + 19.042), & M_V \geq -19.042 \end{cases} \quad (\text{D1})$$

and

$$\Delta m_{gr} = \begin{cases} -0.009, & M_r < -18.873 \\ -0.009 + 0.451(M_r + 18.873), & M_r \geq -18.873 \end{cases} \quad (\text{D2})$$

where $\Delta m_{gV} = m_{g,\text{peak}} - m_{V,\text{peak}}$, $\Delta m_{gr} = m_{g,\text{peak}} - m_{r,\text{peak}}$, and M_V and M_r are the peak absolute magnitudes in their respective filters.

These relations, shown as the red lines in Figure D1, serve as the conversion functions for transforming *V*-band and *r*-band peak absolute magnitudes into the *g*-band baseline used in this work. The scatter from the residuals is 0.12 mag for Δm_{gV} and 0.24 mag for Δm_{gr} .